Check for updates

AGU ADVANCING EARTH AND SPACE SCIENCES

Water Resources Research

RESEARCH ARTICLE

10.1029/2026WR044209

Modeling the Influence of Macro-Roughness on Gravel-Bed River Morphodynamics

Charles M. Shobe[1] **and Daniel N. Scott**[2,3]

[1]U.S. Forest Service Rocky Mountain Research Station, Fort Collins, CO, USA, [2]Riverscape Science and Stewardship, Longmont, CO, USA, [3]Department of Geosciences, Colorado State University, Fort Collins, CO, USA

Key Points:

- Macro-roughness, such as large wood or boulders, influences channel form and evolution
- We present a simple, reach-scale model of macro-roughness-influenced morphodynamics
- Modeling reveals trajectories of channel response to natural and human-driven macro-roughness changes

Correspondence to:

C. M. Shobe,
charles.shobe@usda.gov

Citation:

Shobe, C. M., & Scott, D. N. (2026). Modeling the influence of macro-roughness on gravel-bed river morphodynamics. *Water Resources Research*, *62*, e2026WR044209. https://doi.org/10.1029/2026WR044209

Received 26 MAR 2026
Accepted 27 JUN 2026

Author Contributions:

Conceptualization: Charles M. Shobe, Daniel N. Scott
Formal analysis: Charles M. Shobe
Funding acquisition: Charles M. Shobe
Investigation: Charles M. Shobe, Daniel N. Scott
Methodology: Charles M. Shobe, Daniel N. Scott
Software: Charles M. Shobe
Validation: Charles M. Shobe, Daniel N. Scott
Visualization: Charles M. Shobe
Writing – original draft: Charles M. Shobe
Writing – review & editing: Charles M. Shobe, Daniel N. Scott

© 2026. The Author(s). This article has been contributed to by U.S. Government employees and their work is in the public domain in the USA.
This is an open access article under the terms of the Creative Commons Attribution License, which permits use, distribution and reproduction in any medium, provided the original work is properly cited.

Abstract Gravel-bed rivers adjust their shape in response to environmental changes, including the addition or removal of macro-roughness like logs and boulders. River restoration often involves adding macro-roughness to reduce flow velocity and increase channel-floodplain connectivity, but our understanding of channel response to changes in macro-roughness is limited, in part because of a lack of theory that links macro-roughness to reach-scale channel evolution. We ask how macro-roughness affects gravel-bed river geometry, and how rivers respond to step changes in macro-roughness as might occur during restoration. We develop a process-based model for gravel-bed river evolution that accounts for macro-roughness effects, and explore modeled equilibrium channel form as well as transient response to macro-roughness changes. We also apply the model to a case study from Washington State, USA, where macro-roughness primarily comes from wood loading. Equilibrium simulations reveal three regimes of behavior as roughness increases: one in which modest macro-roughness is predominantly accommodated via bank erosion and widening, one in which greater roughness is accommodated by coupled widening and aggradation/steepening, and one in which overbank flow triggers rapid aggradation that fills the channel. Trajectories of channel response to roughening can be nonmonotonic and nonlinear, implying that perceived effects of roughness changes may differ based on which measurements are made and when. The field case study suggests that the model can be parameterized using data from natural systems, and may, despite inherent simplifications, be useful for conceptualizing how macro-roughness influences the evolution of gravel-bed river shape.

Plain Language Summary Large obstacles like logs, boulders, and beaver dams affect how rivers change their shape over time. Modern river restoration often involves adding obstacles to rivers to reduce flow speed and force water to spill onto the floodplain. Predicting how rivers will respond to these interventions can be difficult. Using a new mathematical model, we explore potential responses of river shape to changes in roughness that might arise from natural processes or human impacts. We find that river response to roughness changes depends primarily on the amount of roughness change and the extent to which obstacles drive flow onto the floodplain. Roughness-driven changes in channels can vary over time; we predict that observed responses to roughness changes will vary based on, among other factors, when measurements are made. Our model may help plan river restoration programs by enabling evaluation of possible responses to restoration in advance.

1. Introduction

The shape of gravel-bed rivers, and the variability in that shape over space and time, control the type and quality of aquatic habitat (Buffington & Montgomery, 2022), the prevalence of fluvial hazards (Eaton et al., 2017; S. Ahrendt et al., 2022), the trajectory of landscape evolution (Gabel et al., 2024; Wickert & Schildgen, 2019), and the response of rivers to human impacts (Gilbert, 1917; Wohl, 2015). On average, gravel-bed river form (bankfull width, depth, and local slope) tends toward a "near-threshold" equilibrium in which the width-averaged bankfull shear stress is slightly greater than the critical shear stress required to move the median bed grain size (Parker, 1978; C. B. Phillips et al., 2022). Channel shape therefore reflects formative conditions including discharge, grain size, sediment supply (Pfeiffer et al., 2017), and flow resistance (Eaton et al., 2004; Francalanci et al., 2020). Physically based regime models derived from near-threshold or similar theory can predict equilibrium channel form under different boundary conditions (Blom et al., 2017; Eaton et al., 2004; Eaton & Millar, 2017; Parker, 1979).

Although gravel-bed river shape obeys the expectations of the near-threshold model in an average sense, making regime models useful for exploring the range of plausible equilibrium channel geometries, it is important to also

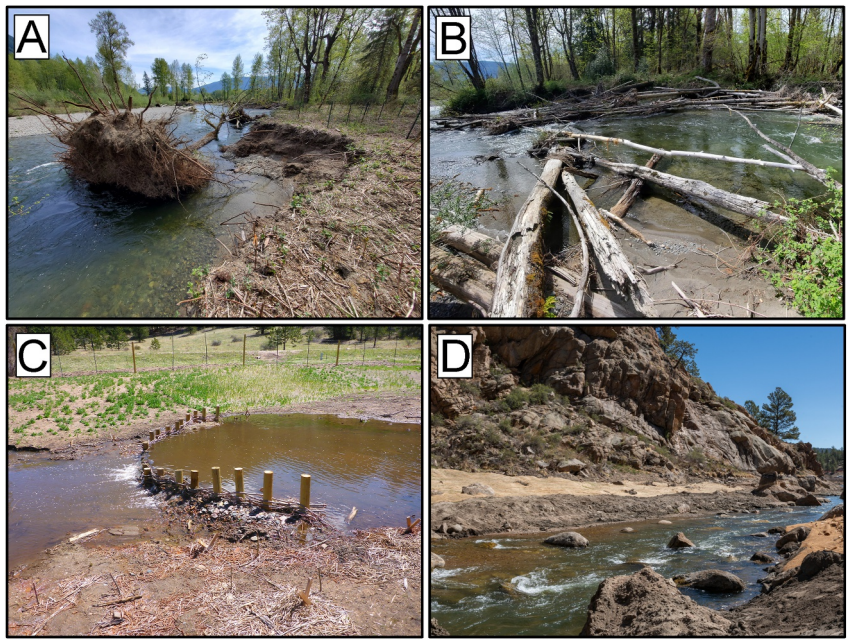

Figure 1. Examples of macro-roughness in gravel-bed rivers. (a) Rootwad-attached log and (b) wood jam on the North Fork Snoqualmie River, WA, USA. (c) Post-assisted log restoration structure on Fish Creek, CO, USA. (d) Boulders in a reach of the South Platte River restored following removal of a small dam. Photos by authors except D, by Erika Reiter, U.S. Forest Service).

understand the timescales and trajectories of transient responses of river shape to changes in formative conditions both to elucidate process dynamics and to enable applied prediction (Davidson & Eaton, 2018; Fryirs, 2017). Rivers respond to natural and human-caused variations in the hydrologic regime (C. B. Phillips et al., 2024), the amount and size of supplied sediment (Abramian et al., 2020; Shobe et al., 2016) and wood (Gurnell et al., 2002; Shields & Gippel, 1995), the density and composition of riparian vegetation (Gurnell, 2014; Wieting et al., 2023), and the actions of animals (Rice, 2021). Humans also directly alter channel morphology and roughness by reshaping the channel (Scott, 2024a; Simon, 1989) and adding or removing in-channel elements ranging from bridge piers (Martín-Vide et al., 2022) to beaver-dam analogs (Davis et al., 2021; Pollock et al., 2014).

Many natural and human-driven changes to channels, and especially river restoration interventions, involve altering the flow resistance of gravel-bed rivers by changing macro-roughness. Macro-roughness elements increase form resistance—the dissipation of energy through pressure drag as the flow interacts with roughness elements like bedforms, boulders, wood, and changing channel cross-section and planform shape (e.g., Kean & Smith, 2006; Millar, 1999; Rickenmann, 2012; Wohl, 2013) (Figure 1). Form resistance, all else equal, takes up more fluid stress as the channel boundary roughens relative to the flow depth (Bathurst, 1978; R. Ferguson, 2007; Powell, 2014; Deal, 2022). Understanding how and how fast gravel-bed rivers adjust to the introduction and removal of macro-roughness is essential to predicting river response to perturbations as diverse as landslides (Shobe et al., 2021; S. M. Ahrendt et al., 2025) and process-based restoration (Ciotti et al., 2021).

Macro-roughness influences local flow and sediment transport dynamics, and in doing so can alter reach-scale channel geometry and planform. Macro-roughness elements like logs, boulders, or leaky barriers effectively constrict the channel cross-section, causing backwater effects such as an elevated water surface and flow deceleration upstream followed by flow acceleration as the flow passes one or more roughness elements (e.g., Addy et al., 2025; Schalko et al., 2018; Zhang et al., 2020). Local variations in the flow field can cause zones of erosion and deposition (Müller et al., 2022; Papanicolaou & Tsakiris, 2017; Wang et al., 2017; You & Tinoco, 2025) even as form drag due to macro-roughness reduces the reach-averaged proportion of fluid stress available to transport sediment (Alzabari et al., 2024; Canovaro et al., 2007; Rickenmann & Recking, 2011; Schneider et al., 2015, 2016; E. Yager et al., 2007). The intensity of these variations correlates with the size and arrangement of macro-roughness elements as well as other variables related to flow, sediment grain size, and channel shape (e.g., Monsalve et al., 2017; L'Hommedieu et al., 2020).

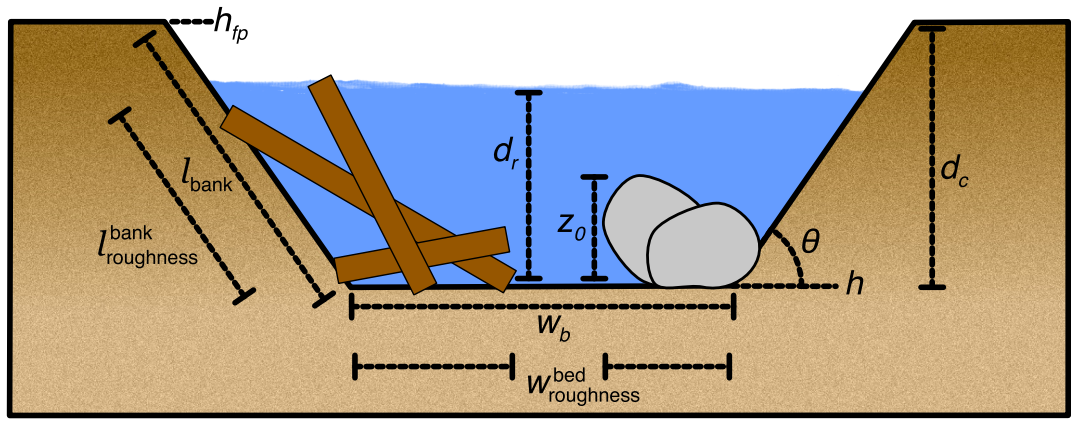

Figure 2. Model definition sketch after Lague (2010). Two potential sources of macro-roughness, large wood (left side) and boulders (right side), are shown. Variables shown are: d_c, channel depth; d_r, flow depth; h, channel bed elevation; h_{fp}, floodplain elevation; θ, bank angle; l_{bank}, bank length; $l^{\text{bank}}_{\text{roughness}}$, length of bank covered by macro-roughness elements; w_b, basal channel width; $w^{\text{bed}}_{\text{roughness}}$, width of the bed covered by macro-roughness elements; z_0, roughness length scale.

Local morphodynamic responses to macro-roughness can alter channel planform by driving bank erosion, bar formation, floodplain reworking, and avulsion, although these effects vary widely across different channel geometry and macro-roughness configurations (Sear et al., 2010; J. D. Phillips, 2012; Zhang & Rutherfurd, 2020; Wohl et al., 2022; Scott, 2024b; Galia & Poledniková, 2025). Understanding how gravel-bed river morphology responds to macro-roughness changes requires accounting for the effects of this complexity at the reach scale. Field case studies of river response to changes in macro-roughness—and particularly the installation of wood structures—are accumulating rapidly (Addy & Wilkinson, 2016; Davis et al., 2021; Maffia et al., 2024; Pearce et al., 2021; Scott, 2024a; Wolstenholme et al., 2024), but limited numbers of observations and widely varying field conditions have prevented development of general theory that goes beyond the equilibrium expectations of regime models (Eaton & Millar, 2017; Francalanci et al., 2020).

Here we ask how macro-roughness affects gravel-bed river geometry, and how rivers respond to changes in macro-roughness. We integrate hydraulic and geomorphic theory to develop a process-based model for gravel-bed river evolution in the presence of macro-roughness, and use it to investigate trajectories and timescales of channel response to macro-roughness changes. We apply the model to a field example to assess similarities and differences between modeled and measured river response to changing macro-roughness.

2. Methods

2.1. Model Dimensionality and Domain

The model evolves a cross-section (Figure 2) representing a reach that extends many channel widths in the upstream-downstream direction such that flow can be assumed to be steady and uniform (E. M. Yager et al., 2018). Channel width and depth are computed as reach-averaged quantities. The model is therefore 0-dimensional as it does not evolve the channel explicitly along any spatial coordinate.

2.2. Model Development

The channel is assumed to maintain a trapezoidal cross-section (e.g., Davidson & Eaton, 2018; Lague, 2010; Stark, 2006) as its width, depth, and local slope change. It has basal width w_b, flow depth d_r, and a constant bank angle θ. Channel depth d_c is the difference between a fixed floodplain elevation h_{fp} and the freely evolving bed elevation h. The channel bed elevation h is compared to a baselevel, or fixed elevation h_{bl}, in the reach immediately downstream to calculate local bed slope S in the reach of interest such that $S = \frac{h - h_{bl}}{L}$ where L is the reach length. S is conceptually the local slope that connects the roughness-influenced reach to its fixed downslope boundary condition and is influenced by local aggradation and incision within the roughness-influenced reach, rather than being the regional slope which is unaffected by local aggradation and incision.

2.2.1. Hydraulics

The key hydraulic assumptions are that (a) flow is steady and uniform, (b) macro-roughness can be expressed as a single roughness length scale that describes the average roughness state of the channel bed (see Houseago et al. (2025) for limits to the validity of this assumption), and (c) overbank flow spreads across a wide floodplain and does not contribute to shaping the channel. To evolve the channel reach cross-section over time, we calculate the effective boundary shear stress (Schneider et al., 2015):

$$\tau_r = \rho_w g R_r S_r \tag{1}$$

where ρ_w is the density of water, g is acceleration due to gravity, and the subscript r denotes—throughout this derivation—the presence of macro-roughness. τ_r, R_r, and S_r are therefore the boundary shear stress, hydraulic radius, and energy slope (see Equation 5 below), respectively, after accounting for macro-roughness. In the absence of any macro-roughness, Equation 1 is equivalent to the commonly used boundary shear stress $\tau = \rho_w g R S$ where R is the hydraulic radius and S is the local bed slope.

The hydraulic radius R_r for a steady, uniform flow is geometrically related to flow depth and basal width in the trapezoidal channel:

$$R_r = \frac{\left(w_b + \frac{d_r}{\tan\theta}\right) d_r}{w_b + 2\frac{d_r}{\sin\theta}}. \tag{2}$$

The flow depth for any discharge Q is initially unknown, but the two are related through continuity using the Darcy-Weisbach flow resistance equation with friction factor f_r:

$$Q = A_r U_r = \left(w_b + \frac{d_r}{\tan\theta}\right) d_r \sqrt{\frac{8 g R_r S_r}{f_r}}. \tag{3}$$

where $A_r = \left(w_b + \frac{d_r}{\tan\theta}\right) d_r$ is the flow cross-section area and $U_r = \sqrt{\frac{8 g R_r S_r}{f_r}}$ is the reach-averaged flow velocity.

The flow-resistance term $\sqrt{\frac{8}{f_r}}$ can be found using the Variable-Power Equation of R. Ferguson (2007), which combines a Manning-Strickler resistance relation for deep (low roughness) flows and a roughness-layer resistance relation for shallow (high roughness) flows and is therefore a widely used way to approximate flow resistance across a wide range of relative roughness conditions including very rough flows (e.g., Rickenmann, 2012; Schneider et al., 2015, 2016; R. Ferguson & Recking, 2025):

$$\sqrt{\frac{8}{f_r}} = \frac{a_1 a_2 (R_r/z_0)}{\sqrt{a_1^2 + a_2^2 (R_r/z_0)^{5/3}}}. \tag{4}$$

Here a_1 and a_2 are constants with values of 7 and 3, respectively, found to provide the best fit to data by R. Ferguson and Recking (2025). z_0 is a hydraulic roughness length scale that incorporates the effects of both grain roughness and macro-roughness elements (logs, boulders, beaver dam analogs, etc.). Rather than calculate hydraulic effects of macro-roughness using stress partitioning with explicit representations of roughness elements (e.g., Smith et al., 2011) or assumed distributions of roughness element size, shape, and spacing (Kean & Smith, 2006; E. Yager et al., 2007; Shobe et al., 2016), we take a simpler approach in which all roughness in the channel is incorporated into the roughness length scale z_0.

The energy slope of the flow in the presence of macro-roughness is found by calculating the effective energy slope, which is less than the local bed slope by a proportion determined by the ratio of base-level to total friction factor (Rickenmann, 2012; Rickenmann & Recking, 2011; Schneider et al., 2015):

$$S_r = S\left(\sqrt{\frac{f}{f_r}}\right)^e. \tag{5}$$

Here f is the base-level friction factor (*sensu* Rickenmann & Recking, 2011; Rickenmann, 2012) that describes flow resistance without contributions from macro-roughness, f_r is the total friction factor that includes the effects of macro-roughness, and e has a value between 1.2 and 2 (Chiari & Rickenmann, 2011; Meyer-Peter & Müller, 1948; Nitsche et al., 2011). When $f \approx f_r$, effects of macro-roughness on energy slope are negligible such that $S_r \approx S$.

The base-level friction factor f is found by extrapolating a Manning-Strickler resistance relation, which applies to flows with high relative submergence R_r/z_0 (low relative roughness), to flows of any relative submergence (Rickenmann, 2012; Schneider et al., 2015):

$$\sqrt{\frac{8}{f}} = a_1 (R_r/z_0)^{1/6}. \tag{6}$$

Combining Equations 2–6 allows for an iterative solution for d_r (see Appendix A for derivation):

$$Q = \left(w_b + \frac{d_r}{\tan\theta}\right) d_r \frac{a_1 a_2 \left(\frac{\left(w_b + \frac{d_r}{\tan\theta}\right) d_r}{w_b + 2\frac{d_r}{\sin\theta}} / z_0\right)}{\sqrt{a_1^2 + a_2^2 \left(\frac{\left(w_b + \frac{d_r}{\tan\theta}\right) d_r}{w_b + 2\frac{d_r}{\sin\theta}} / z_0\right)^{5/3}}} \sqrt{g \frac{\left(w_b + \frac{d_r}{\tan\theta}\right) d_r}{w_b + 2\frac{d_r}{\sin\theta}} S \left(\frac{a_2 \left(\frac{\left(w_b + \frac{d_r}{\tan\theta}\right) d_r}{w_b + 2\frac{d_r}{\sin\theta}} / z_0\right)^{5/6}}{\sqrt{a_1^2 + a_2^2 \left(\frac{\left(w_b + \frac{d_r}{\tan\theta}\right) d_r}{w_b + 2\frac{d_r}{\sin\theta}} / z_0\right)^{5/3}}} \right)^e}, \tag{7}$$

which enables calculation of the hydraulic radius R_r Equation 2, friction factor f_r Equation 4, and boundary shear stress τ_r Equation 1. If flow depth d_r exceeds the channel depth d_c (the height of the floodplain surface above the thalweg), we assert that $d_r = d_c$ (Figure 2). This assumes that any remaining discharge after filling the channel spreads out over a wide floodplain and does not contribute to shaping the channel. The alternative would be to route flow across the floodplain in addition to the channel, which would add significant model complexity.

2.2.2. Sediment Transport

We assume that changes in sediment volume in the channel reach result from imbalances in sediment fluxes into $\left(Q_s^{\text{in}}\right)$ and out of $\left(Q_s^{\text{out}}\right)$ the reach, and also that shielding of the bed and/or banks by macro-roughness elements can reduce sediment flux out of the reach. The latter assumption accounts for protection of the bed and banks from erosion where roughness elements are in contact with the channel boundary. Sediment entrainment due to flow acceleration when roughness elements are near, but not in contact with, the boundary (i.e., scour; Zhang & Rutherfurd, 2020) is assumed to be captured in an average sense by the bedload transport relation but cannot be calculated explicitly because the spatial distribution of roughness elements is not modeled. Q_s^{in} is a boundary condition. Q_s^{out} is calculated using the Meyer-Peter and Müller (1948) bedload transport formula (Wickert & Schildgen, 2019)—with corrected constants from Wong and Parker (2006)—that we have also modified to account for limited availability of mobile sediment due to shielding by macro-roughness elements:

$$Q_s^{\text{out}} = \begin{cases} 3.97\left(\frac{\rho_s - \rho_w}{\rho_w}\right)^{1/2} g^{1/2}\left(\tau_r^* - \tau_c^*\right)^{3/2} D_{50}^{3/2} w_r \left(1 - f_c^{\text{tot}}\right) & \text{if } \tau_r^* > \tau_c^* \\ 0 & \text{if } \tau_r^* \leq \tau_c^* \end{cases} \tag{8}$$

Here ρ_s is the sediment grain density, D_{50} is the median grain diameter, τ_r^* is the Shields stress:

$$\tau_r^* = \frac{\tau_r}{\left(\rho_s - \rho_w\right) g D_{50}}, \tag{9}$$

and w_r is the flow width calculated using the trapezoidal channel geometry:

$$w_r = w_b + 2\frac{d_r}{\tan\theta}. \tag{10}$$

The critical Shields stress τ_c^* required to initiate sediment transport is 0.0495 (Wong & Parker, 2006). The $\left(1 - f_c^{\text{tot}}\right)$ term is added for this study to incorporate the effects of shielding that are likely to be present in systems with macro-roughness (E. Yager et al., 2007). f_c^{tot} is the fraction of the channel boundary from which sediment cannot be entrained because it is shielded by roughness elements. In general, bedload transport relations like Equation 8 are thought to reasonably describe transport in streams with rough beds provided that the boundary shear stress is reduced to account for macro-roughness (e.g., E. Yager et al., 2007; Rickenmann & Recking, 2011; Nitsche et al., 2011; Schneider et al., 2015) as we have done here.

2.2.3. Morphodynamics

To enable morphologic adjustment of both the channel bed and banks to changing macro-roughness, we partition the effective boundary shear stress τ_r between the bed and banks. The assumptions underlying this approach are that (a) channel banks can erode whenever bedload can be entrained from the bed, and (b) banks erode in proportion to the stress exerted on them. This is broadly consistent with studies showing that bank erosion is associated with mobility of the channel bed (Nanson & Hickin, 1986) even in streams where the banks undergo mass failure rather than scour alone (e.g., Darby et al., 2010). Stress partitioning is an important component of the model because it ensures that there are limits to channel narrowing (which increases bank stress) and widening (which decreases bank stress), but there is no agreed-upon best practice for stress partitioning in alluvial rivers (T. Li et al., 2022). We follow Lague (2010) in partitioning stresses between the bed and banks using the empirical approach of Flintham and Carling (1988):

$$\tau_{\text{bank}} = \tau_r \frac{F_w}{2}\left(\frac{w_b}{d_r}\sin\theta + \cos\theta\right) \tag{11}$$

$$\tau_{\text{bed}} = \tau_r(1 - F_w)\left(1 + \frac{d_r}{w_b\tan\theta}\right) \tag{12}$$

where F_w is the proportion of shear force exerted on the banks, given by:

$$F_w = 1.766\left(\frac{w_b}{2d_r}\sin\theta + 1.5\right)^{-1.4026}. \tag{13}$$

Use of this stress-partitioning method restricts model applicability to channels with bank angle $\theta > 45°$ (Flintham & Carling, 1988). The key feature of this approach, as with other empirically derived approaches we could have used (e.g., T. Li et al., 2022), is that F_w decreases as the width/depth ratio increases and vice versa. Different stress-partitioning empiricisms would, with all else held equal, be unlikely to affect the general influence of macro-roughness on channel form, although they would affect equilibrium channel geometries and the magnitude of responses to changes in macro-roughness.

Equations 11 and 12 can be linked to the channel-reach mass balance using a set of erosion rate laws. Assuming that all Q_s^{in} aggrades on the bed and/or banks and that all Q_s^{out} is sourced from the bed and/or banks, we can write a pair of mass conservation equations:

$$\frac{Q_s^{\text{in}}}{L} = D_{\text{bed}}w_b + D_{\text{bank}}2l_{\text{bank}} \tag{14}$$

and

$$\frac{Q_s^{\text{out}}}{L} = E_{\text{bed}}w_b + E_{\text{bank}}2l_{\text{bank}}. \tag{15}$$

Here L is the length of the reach and E and D are the surface-normal sediment erosion and deposition rates (volume of sediment per unit surface area), respectively, on each surface. $2l_{\text{bank}}$ is the total cross-stream length of the banks and $l_{\text{bank}} = \frac{d_c}{\sin\theta}$, such that the model tracks the average position of the entire bank. Equations 14 and 15 describe a transport-limited system in which sediment from the channel boundary is always available to be moved if there is sufficient stress to move it.

The final constraint allowing calculation of erosion and deposition rates comes from the assumption that the ratio of rates between the bed and banks is a function of the shear stress on each surface, a dimensionless rate constant (k^*_{dep} and k^*_{ero}), and the fraction of the surface not protected by macro-roughness elements:

$$\frac{D_{\text{bed}}}{D_{\text{bank}}} = k^*_{\text{dep}} \frac{\tau^a_{\text{bank}}\left(1 - f_c^{\text{bank}}\right)}{\tau^a_{\text{bed}}\left(1 - f_c^{\text{bed}}\right)} \tag{16}$$

$$\frac{E_{\text{bed}}}{E_{\text{bank}}} = k^*_{\text{ero}} \frac{\tau^a_{\text{bed}}\left(1 - f_c^{\text{bed}}\right)}{\tau^a_{\text{bank}}\left(1 - f_c^{\text{bank}}\right)}. \tag{17}$$

Here a is an exponent set to 3/2 for consistency with the sediment transport function we employ (Meyer-Peter & Müller, 1948; Wong & Parker, 2006), and f_c^{bank} and f_c^{bed} are the cover fractions of the banks and bed, respectively. Equations 16 and 17 partition deposition and erosion, respectively, between the bed and banks, allocating the gain or loss of sediment in the reach that is determined by the divergence of Q_s^{in} and Q_s^{out}. Equations 16 and 17 need not be related to the form of the sediment transport function, although it is intuitive that they might be given that the same forces entraining sediment might play a role in partitioning erosion/deposition between the bed and banks. Equation 16 as written implies that cover of a particular surface drives deposition on that surface, which might be reasonable if macro-roughness elements are expected to trap sediment. Alternatively, the cover terms could be removed from Equation 16.

The bed and bank cover fractions are geometrically related to the total cover fraction f_c^{tot}:

$$f_c^{\text{tot}} = \frac{f_c^{\text{bed}} w_b + f_c^{\text{bank}} 2l_{\text{bank}}}{2l_{\text{bank}} + w_b}, \tag{18}$$

and are calculated by dividing the cross-stream length of bed and banks covered by macro-roughness elements ($w^{\text{bed}}_{\text{roughness}}$ and $l^{\text{bank}}_{\text{roughness}}$, respectively; these are model parameters) by the cross-stream length of the bed and banks (w_b and l_{bank}, respectively; these freely evolve in the model):

$$f_c^{\text{bed}} = \frac{w^{\text{bed}}_{\text{roughness}}}{w_b} \tag{19}$$

and

$$f_c^{\text{bank}} = \frac{l^{\text{bank}}_{\text{roughness}}}{l_{\text{bank}}}. \tag{20}$$

The cross-sectional area blockage ratio, a commonly measured quantity in the field describing the proportion of the channel that is obstructed by macro-roughness elements (e.g., Gippel et al., 1996), is likely to be proportional to $w^{\text{bed}}_{\text{roughness}}$ and $l^{\text{bank}}_{\text{roughness}}$ for most common types of macro-roughness.

The two dimensionless rate constants k^*_{dep} and k^*_{ero} in Equations 16 and 17 are important model parameters. Each constant scales the relative efficiency of deposition (erosion) between the bed and banks. Values near unity mean that deposition (erosion) does not occur preferentially on the bed or banks, values $\gg 1$ indicate that deposition

(erosion) occurs preferentially on the bed, and values ≪1 mean that deposition (erosion) occurs preferentially on the banks. The two constants probably should not have similar values; it is likely that $k^*_{\text{dep}} \gg k^*_{\text{ero}}$ because deposition occurs preferentially on the bed while erosion occurs on both the bed and banks (Parker, 1978).

The erosion and deposition rates can be found by combining Equations 14–17 to solve for four unknowns (D_{bed}, D_{bank}, E_{bed}, and E_{bank}):

$$D_{\text{bed}} = \frac{Q_s^{\text{in}}}{L\left(\frac{1}{k^*_{\text{dep}}}\frac{\tau^a_{\text{bed}}\left(1-f_c^{\text{bed}}\right)}{\tau^a_{\text{bank}}\left(1-f_c^{\text{bank}}\right)}2l_{\text{bank}} + w_b\right)} \tag{21}$$

$$D_{\text{bank}} = \frac{Q_s^{\text{in}}}{L\left(k^*_{\text{dep}}\frac{\tau^a_{\text{bank}}\left(1-f_c^{\text{bank}}\right)}{\tau^a_{\text{bed}}\left(1-f_c^{\text{bed}}\right)}w_b + 2l_{\text{bank}}\right)} \tag{22}$$

$$E_{\text{bed}} = \frac{Q_s^{\text{out}}}{L\left(\frac{1}{k^*_{\text{ero}}}\frac{\tau^a_{\text{bank}}\left(1-f_c^{\text{bank}}\right)}{\tau^a_{\text{bed}}\left(1-f_c^{\text{bed}}\right)}2l_{\text{bank}} + w_b\right)} \tag{23}$$

$$E_{\text{bank}} = \frac{Q_s^{\text{out}}}{L\left(k^*_{\text{ero}}\frac{\tau^a_{\text{bed}}\left(1-f_c^{\text{bed}}\right)}{\tau^a_{\text{bank}}\left(1-f_c^{\text{bank}}\right)}w_b + 2l_{\text{bank}}\right)}. \tag{24}$$

Surface-normal rates of surface change on the bed and banks, $\frac{\partial h_{\text{bed}}}{\partial t}$ and $\frac{\partial h_{\text{bank}}}{\partial t}$, respectively, arise from the balance between erosion and deposition on each surface:

$$\frac{\partial h_{\text{bed}}}{\partial t} = \frac{D_{\text{bed}} - E_{\text{bed}}}{1-\phi} \tag{25}$$

$$\frac{\partial h_{\text{bank}}}{\partial t} = \frac{D_{\text{bank}} - E_{\text{bank}}}{1-\phi}, \tag{26}$$

where ϕ is the porosity of the bed and bank material.

Bed elevation and channel width are then explicitly solved forward in time to reflect erosion and/or deposition. Bed elevation at time $t + 1$ is found by:

$$h^{\text{t}+1} = h^{\text{t}} + \frac{\partial h_{\text{bed}}}{\partial t}\Delta t, \tag{27}$$

and channel depth is updated by subtracting $h^{\text{t}+1}$ from the constant floodplain elevation h_{fp}. Basal channel width at time $t + 1$ is:

$$w_b^{\text{t}+1} = w_b^{\text{t}} + 2\left(\frac{-\frac{\partial h_{\text{bank}}}{\partial t}}{\sin\theta} + \frac{\frac{\partial h_{\text{bed}}}{\partial t}}{\tan\theta}\right)\Delta t, \tag{28}$$

where the two terms in the parentheses are the contributions to width change of bank and bed evolution, respectively (Lague, 2010). Local bed slope is adjusted after each timestep by comparing the updated bed elevation to the steady downstream baselevel at the downstream end of the reach:

$$S^{\text{t}+1} = \frac{h^{\text{t}+1} - h_{bl}}{L}. \tag{29}$$

Table 1
Parameter Values and Ranges Used for Exploratory Simulations

Parameter	Value
θ	60°
e	1.5
k^*_{ero}	1
k^*_{dep}	10
z_0	0.01–10 m
$w^{\mathrm{bed}}_{\mathrm{roughness}}$	0–120 m
$l^{\mathrm{bank}}_{\mathrm{roughness}}$	0–5 m
h_{fp}	10.6 m (initial $d_c = 5$ m)
Q	150 m^3/s
Q^{in}_s	0.001 m^3/s
D_{50}	0.06 m
ϕ	0.3
L	1,000 m
dt	1,000 s

2.3. Numerical Experiments

First, we explore the effects of macro-roughness on modeled equilibrium channel geometry and quantify trajectories and timescales of channel response to changes in macro-roughness (Section 2.3.1). We then apply the model to a field case study (Section 2.3.2).

2.3.1. Exploratory Experiments

To investigate general model behavior, we explore the effects of changes in roughness length scale (z_0), bank cover ($l^{\mathrm{bank}}_{\mathrm{roughness}}$), and bed cover ($w^{\mathrm{bed}}_{\mathrm{roughness}}$). We parameterize the model using values that are reasonable for gravel-bed rivers but not tied to any specific field site and are selected to illustrate the range of potential model behavior (Table 1). We set the erosion and deposition constants to $k^*_{\mathrm{ero}} = 1$ and $k^*_{\mathrm{dep}} = 10$, respectively, reasoning that deposition is disproportionately focused on the bed over the banks relative to erosion. Equilibrium conditions are defined as occurring when both width and local slope remain within a small relative tolerance across two successive timesteps such that $|w_b^{t+1} - w_b^t| <= 2 \times 10^{-13}\Delta t$ and $|S^{t+1} - S^t| <= 2 \times 10^{-13}\Delta t$. We begin all simulations from the equilibrium width and slope of a baseline low-roughness model case defined by $z_0 = 0.01$ m, $l^{\mathrm{bank}}_{\mathrm{roughness}} = 0$ m, and $w^{\mathrm{bed}}_{\mathrm{roughness}} = 0$ m, such that these experiments assess equilibrium form and transient adjustment in response to increases in z_0, $l^{\mathrm{bank}}_{\mathrm{roughness}}$, and $w^{\mathrm{bed}}_{\mathrm{roughness}}$ caused by macro-roughness.

2.3.2. Application to a Field Example

To investigate how the model might be parameterized and applied to a natural river, we use a field case study on the South Fork Snoqualmie River, a meandering gravel-bed river in Washington State, USA that experiences hydraulic roughness due to large-wood loading (Figure 3). This is not a complete model calibration/validation exercise *sensu* Barnhart et al. (2020a), but rather an initial exploration of the extent to which the model might apply to a real system.

Our study reach, which drains approximately 212 km^2, was chosen because we have repeat aerial imagery and topobathymetric LiDAR digital elevation models (DEMs) for the period between 2019 and 2024, allowing us to constrain many of the variables relevant to the model. The study reach is located immediately upstream from the confluence of the South Fork with the Middle Fork Snoqualmie River, and exhibits mostly single-thread, pool-riffle morphology. The study site is located approximately 2 km downstream from USGS discharge gage #12144000 (Figure 3b) (U.S. Geological Survey, 2026). The average discharge during the 2019–2024 period was approximately 14 m^3/s; flow peaks of up to about 250 m^3/s occurred during the autumn and winter seasons of 2019–2024 (Figure 3b).

We have imagery and DEMs (Figures 3c–3f) from 2019, 2020, 2022, and 2024, allowing us to estimate z_0, $w^{\mathrm{bed}}_{\mathrm{roughness}}$, and $l^{\mathrm{bank}}_{\mathrm{roughness}}$. This data set also enables measurement of channel geometry, yielding width and bed elevation data that can be used to initialize the model in 2019 and compare modeled with measured channel geometry over subsequent surveys in 2020, 2022, and 2024. Our experiment is structured such that the 2019 data are initial conditions. Wood-related parameters z_0, $w^{\mathrm{bed}}_{\mathrm{roughness}}$, and $l^{\mathrm{bank}}_{\mathrm{roughness}}$ are updated in 2020 and 2022. 2020, 2022, and 2024 morphologic data (w_b and h) are not used to update the model but rather are compared against modeled w_b and h to assess model-data misfit.

We parameterize the model, and develop a set of initial conditions, from aerial imagery and topobathymetry (Table 2). Basal channel width w_b is measured by drawing a polygon for each survey year with fixed upstream and downstream edges that follows the channel bank tops (this is a slight overestimation of basal width because the channel banks are not vertical, but the difference is negligible relative to the channel width; Figures 3c–3f), then dividing that polygon's area by the along-channel polygon length ($L = 1100.2$ m, Table 2), which remained

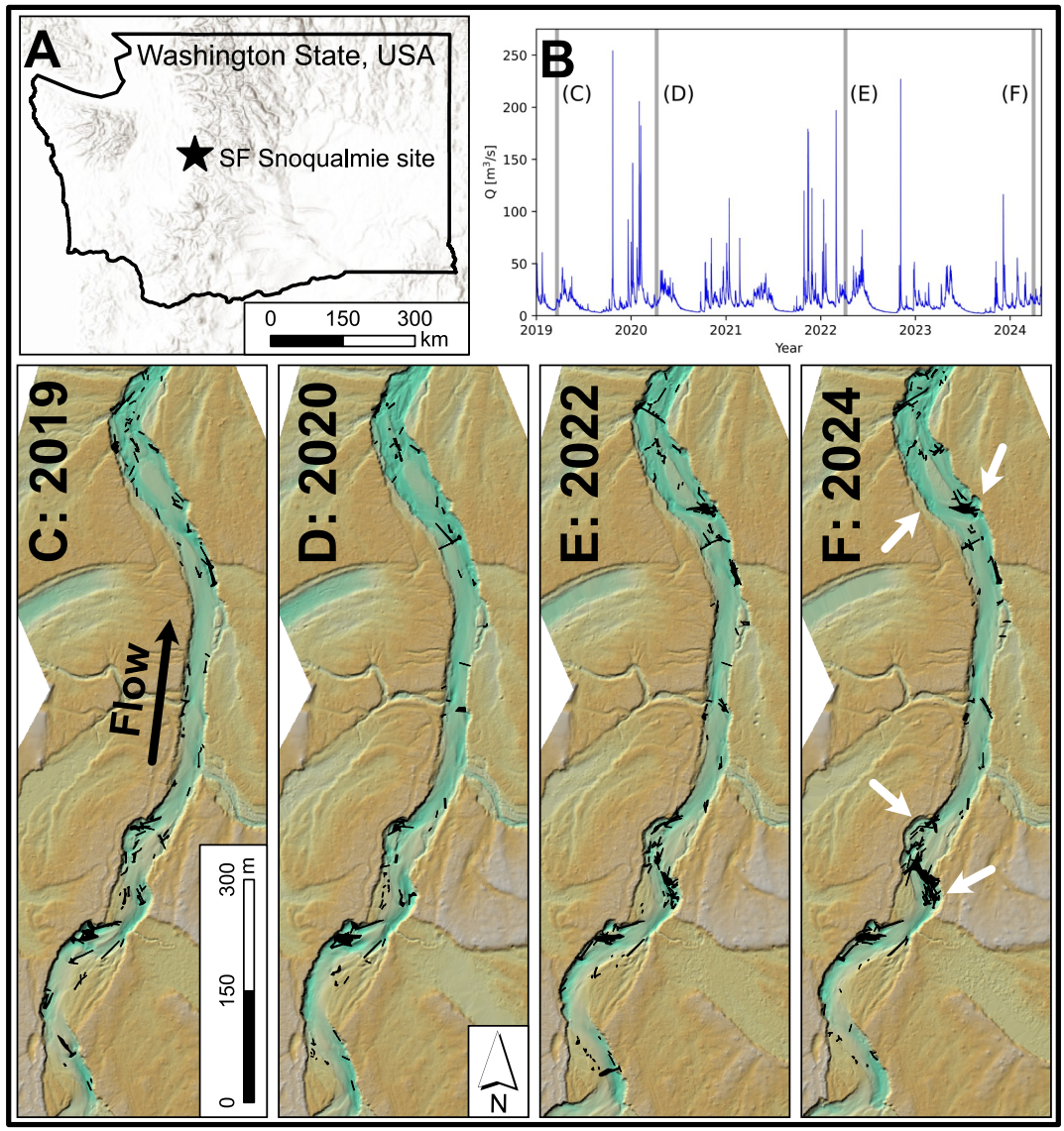

Figure 3. Case study location and site context. (a) location of the SF Snoqualmie site in Washington, USA. (b) Hydrograph over the study period from USGS gage #12144000 at North Bend, WA. Gray lines indicate times of lidar-derived topobathymetry shown in (c–f). Black polygons in (c–f) show large wood traced from aerial imagery. White arrows in (f) show areas of noticeable bank erosion associated with wood loading. The total relief in (c–f) is approximately 8 m.

constant across survey years. This yields a mean w_b value along the study section. Channel bed elevation h is measured by averaging elevation values across the channel bed at the upstream end of the study reach from each survey year's topobathymetric DEM. Downstream baselevel bed elevation h_{bl} is measured by averaging elevation values across the channel bed just downstream of the study reach. Local slope is then the elevation difference between h and h_{bl}, divided by the reach length. The floodplain elevation h_{fp} is found by averaging elevation values in a polygon drawn on the floodplain; the channel depth d_c is $h_{fp} - h$.

We calculate a reach-averaged value for the cross-stream length of the bed covered by wood $\left(w_{\text{roughness}}^{\text{bed}}\right)$ by measuring f_c^{bed}, the proportion of the study reach polygon covered with large wood, and multiplying f_c^{bed} by the channel width w_b to yield an along-channel average $w_{\text{roughness}}^{\text{bed}}$. We calculate the reach-averaged cross-stream bank length covered by wood $\left(l_{\text{roughness}}^{\text{bank}}\right)$ by measuring the planview proportion of the banks that is overlapped by large wood (the only dimension of bank cover we can quantify from aerial imagery) and then multiplying that

Table 2
Parameter Values and Ranges Used for Field Case Study Simulations

Parameter	Value
θ	60°
e	1.5
k^*_{ero}	0.01–10
k^*_{dep}	1–120
z_0	0.13–0.14 m (lower-roughness case)
	0.20–0.23 m (higher-roughness case)
$w^{\mathrm{bed}}_{\mathrm{roughness}}$	1.35–1.84 m (see Section 2.3.2)
$l^{\mathrm{bank}}_{\mathrm{roughness}}$	0.61–0.95 m (see Section 2.3.2)
h_{fp}	6.14 m (initial $d_c = 2.95$ m)
Q	USGS gage #12144000 hydrograph
Q^{in}_s	varies with Q (see Section 2.3.2)
D_{50}	0.03 m
ϕ	0.3
L	1,100.2 m
dt	100 s

proportion by cross-stream bank length under the assumption that, on average along the study reach, f^{bank}_c is equal to the planview proportion of wood-affected banks.

There is no single well-established procedure for deriving the roughness length scale z_0, especially given that in our study z_0 reflects the influence not just of bed topography and grain roughness but also of macro-roughness. Given this uncertainty, we assume that z_0 is related to the standard deviation of bed elevation σ_z (R. I. Ferguson et al., 2024; Chen et al., 2025), and that σ_z can be affected by macro-roughness. We derive two sets of z_0 values: a lower-roughness and higher-roughness set, and present results using both sets of values. We calculate z_0 as a spatially weighted average of σ^{base}_z, the roughness length of the bed in areas without any large wood (of area A_{base}), and σ^{wood}_z, the roughness length of the bed in areas with large wood (of area A_{wood}):

$$z_0 = \frac{\sigma^{\mathrm{base}}_z A_{\mathrm{base}} + \sigma^{\mathrm{wood}}_z A_{\mathrm{wood}}}{A_{\mathrm{tot}}}, \tag{30}$$

where $A_{\mathrm{tot}} = A_{\mathrm{base}} + A_{\mathrm{wood}}$. We set σ^{base}_z to 0.12 m, which is the standard deviation of bed elevation of a representative patch of the bed measured from our topobathymetric DEMs. Because our horizontal DEM resolution (0.9 m) is too large to consider this value representative of grain roughness alone, it represents the contributions to roughness of both grains ($D_{50} = 0.03$ m; Booth et al. (1991)) and bedforms, but not large wood. We use $\sigma^{\mathrm{base}}_z = 0.12$ m for both the lower- and higher-roughness cases. Values of σ^{wood}_z carry much more uncertainty; we consider a lower-roughness case in which $\sigma^{\mathrm{wood}}_z = 0.5$ m, a common value for trunk diameter of the large wood in our study site, and a higher-roughness case in which $\sigma^{\mathrm{wood}}_z = 3$ m, which we derived from estimating the diameter of the largest rootwads observed in the imagery. Using these two end-member values for σ^{wood}_z, we calculate spatially averaged z_0 values of 0.13–0.14 m for the lower-roughness case and 0.20–0.23 m for the higher-roughness case. We expect methods for calculating the roughness length scale from field data to evolve as understanding continues to improve (e.g., R. I. Ferguson et al., 2024; Houseago et al., 2025; Chen et al., 2025).

Time-evolving volumetric sediment flux into the reach is calculated by assuming that Q^{in}_s is a power-law function of Q (Lague, 2010):

$$Q^{\mathrm{in}}_s = p_b * kQ^m. \tag{31}$$

Here p_b is the proportion of sediment traveling as bedload which we set to 0.05, a value estimated for the South Fork Snoqualmie River by Nelson (1971), and m is a rating exponent that we set to 2 following Lague (2010). We set the coefficient k to 1.9×10^{-6} s/m^3 to yield bedload supply rates over the study period (range of 1,800–5,000 t/yr during 2019–2024; 3,200 t/yr average) consistent with those estimated from watershed sediment budgets (2,600 t/yr; Reid & Dunne, 1996) and inferred from suspended-sediment measurements (1,000–4,200 t/yr; Nelson, 1971). The Q^{in}_s time series could be improved by replacing Equation 31 with multi-temporal field data or output from bedload transport models calibrated to the field area. Meaningfully different Q^{in}_s values could change modeled outcomes, for example, by influencing whether the channel experiences a positive or negative sediment mass balance.

The two model parameters that cannot be reasonably estimated a priori are the dimensionless erosion and deposition constants k^*_{ero} and k^*_{dep}, respectively. We therefore search for best-fit values of k^*_{ero} and k^*_{dep} by comparing modeled and measured w_b values in 2020, 2022, and 2024 (the 2019 w_b value serves as the model's initial condition and so is not used to calculate misfit) using the misfit function:

$$\mu = \frac{1}{N}\sqrt{\sum_{i=1}^{N}\frac{\left(w_b^{\text{obs}} - w_b^{\text{sim}}\right)^2}{\delta^2}} \tag{32}$$

where μ is total misfit, $N = 3$ observations (2020, 2022, and 2024 surveys), w_b^{obs} is the observed width from each survey, w_b^{sim} is the simulated width at the time of each survey, and $\delta = 2.5$ m is a rough estimate of the uncertainty on our width measurements. We use the differential evolution optimization algorithm (Storn & Price, 1997) to find the values of k_{ero}^* and k_{dep}^* that minimize misfit between modeled and measured channel width. Table 2 gives the ranges of k_{ero}^* and k_{dep}^* over which we searched for best-fit values.

3. Results

3.1. Macro-Roughness Effects on Equilibrium Channel Geometry

Macro-roughness elements have three possible effects in our model: they increase the hydraulic roughness length scale z_0, the width of the bed protected from flow stress $w_{\text{roughness}}^{\text{bed}}$, and the cross-stream length of the banks protected from flow stress $l_{\text{roughness}}^{\text{bank}}$. Here we show how modeled channels respond to these three effects, and how variations in the erosion and deposition coefficients k_{ero}^* and k_{dep}^*, respectively, influence results.

3.1.1. Influence of Increasing Roughness

Roughening the channel enlarges the equilibrium cross-section (Figure 4), increasing the basal channel width (Figure 4a) and flow depth (Figure 4b) in concert such that the ratio of basal width to depth remains nearly constant. Local bed slope, which is directly coupled to bed aggradation/incision and represents the drop along the thalweg from the modeled reach to its downstream baselevel, declines only very slightly as z_0 increases from 0.01 to 0.3 m, followed by an increase with z_0 for $z_0 > 0.3$ m (Figure 4c; squares). Effective energy slope, which incorporates the loss of transport capacity due to macro-roughness, declines monotonically with increasing roughness (Figure 4c; triangles). Equilibrium bank and bed shear stresses remain nearly constant across the range of z_0 (Figure 4d). The ratio of friction factors f_r/f, a measure of the friction added by macro-roughness, remains near 1 for $z_0 < 0.1$ m, then increases with z_0 for $z_0 > 0.1$ m (Figure 4e). Our exploration of the roughness parameter space spans relative submergence (R_r/z_0) values from 0.34 to 88.6 (Figure 4f), covering almost the entire range of conditions captured by hydraulic data sets (e.g., Deal, 2022; R. Ferguson & Recking, 2025).

Interactions among roughness, channel geometry, and overbank flow give rise to three regimes of behavior labeled in Figure 4a. In the widening-dominated regime observed at low relative roughness ($z_0 < 0.4$ m; $R_r/z_0 > 4$), roughening increases channel width (Figure 4a) without much affecting bed elevation and therefore local slope (Figures 4b and 4c, respectively). This regime is associated with f_r/f ratios close to 1 (Figure 4e). Moderate relative roughness ($0.4 < z_0 < 2$ m; $4 > R_r/z_0 > 1$) causes the channel to enter the widening/steepening regime, defined by coupled increases in width, bed elevation/local slope, and f_r/f. The widening/steepening regime encompasses all $z_0 > 0.4$ m (and all $R_r/z_0 < 1$) in Figure 4 when the channel banks are assumed to be high enough to contain all flow (i.e., flow cannot go overbank; translucent markers in Figure 4).

When we relax the assumption that the channel's bankfull depth is much greater than the maximum flow depth (i.e., when the channel depth d_c is less than the maximum flow depth), we find that overbank flow driven by high roughness ($z_0 > 2$ m and $R_r/z_0 < 1$ in Figure 4) can cause runaway channel filling. There is no equilibrium channel geometry in the filling regime. The translucent markers in Figure 4 indicate equilibrium conditions that would be achieved in the absence of overbank flow; these would be characteristic of the widening/steepening regime.

Regime boundaries are not fixed at the specific z_0 or R_r/z_0 values at which they occur in Figure 4; rather, they are set by interactions among roughness, floodplain elevation, discharge, incoming sediment flux, and initial channel geometry. For example, shallower channels—those that have floodplains not much higher than their beds—enter the filling regime at lower values of z_0 than deeper channels do.

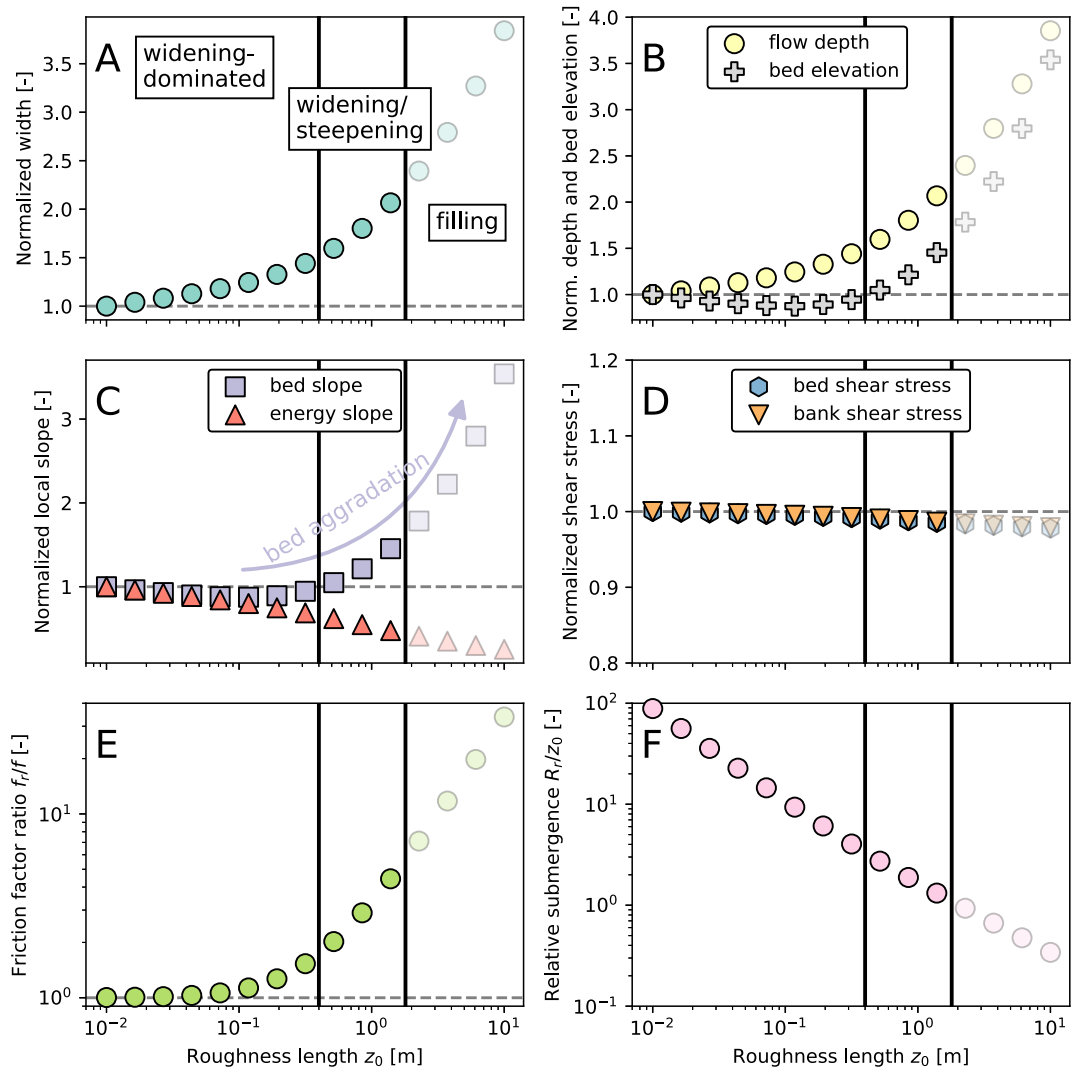

Figure 4. Influence of roughness length z_0 on equilibrium channel width (a), flow depth and bed elevation (b), bed and energy slope (c), bed and bank shear stress (d), friction factor (e), and relative submergence (f) with all other parameters held constant. In (a–d), quantities are normalized to their values in the low-roughness end-member ($z_0 = 0.01$ m). Gray dashed lines show values of 1. To illustrate the effects of macro-roughness alone, the bed cover terms $w_{\text{roughness}}^{\text{bed}}$ and $l_{\text{roughness}}^{\text{bank}}$ are set to 0 here. Translucent points (the filling regime) represent equilibrium values that the model would achieve in the absence of overbank flow and resulting channel filling.

3.1.2. Influence of Increasing Bed and Bank Cover

Increasing bed cover, all else held equal, drives channel widening (Figure 5a), bed aggradation and flow shallowing (Figure 5b), and increases in both the local bed slope and energy slope (Figure 5c). Bed shear stress remains constant as the bed cover fraction increases; the increased bed cover is accommodated by large decreases in bank shear stress as the channel widens (Figure 5d). The friction factor ratio increases slightly (Figure 5e) and relative submergence decreases slightly (Figure 5f) as channel widening causes the flow to become shallower while z_0 remains fixed.

Increasing bank cover causes morphologic responses that are opposite to those caused by increasing bed cover. The channel narrows (Figure 6a), the flow deepens and the bed incises (Figure 6b), and both the local bed slope and energy slope decline (Figure 6c). As in the experiments that increased bed cover, bank shear stress shows a much stronger response than bed shear stress (Figure 6d). Bed shear stress declines very slightly with bank cover for values $0 < f_c^{\text{bank}} < 0.6$, and then more strongly for $f_c^{\text{bank}} > 0.6$, while bank shear stress increases strongly

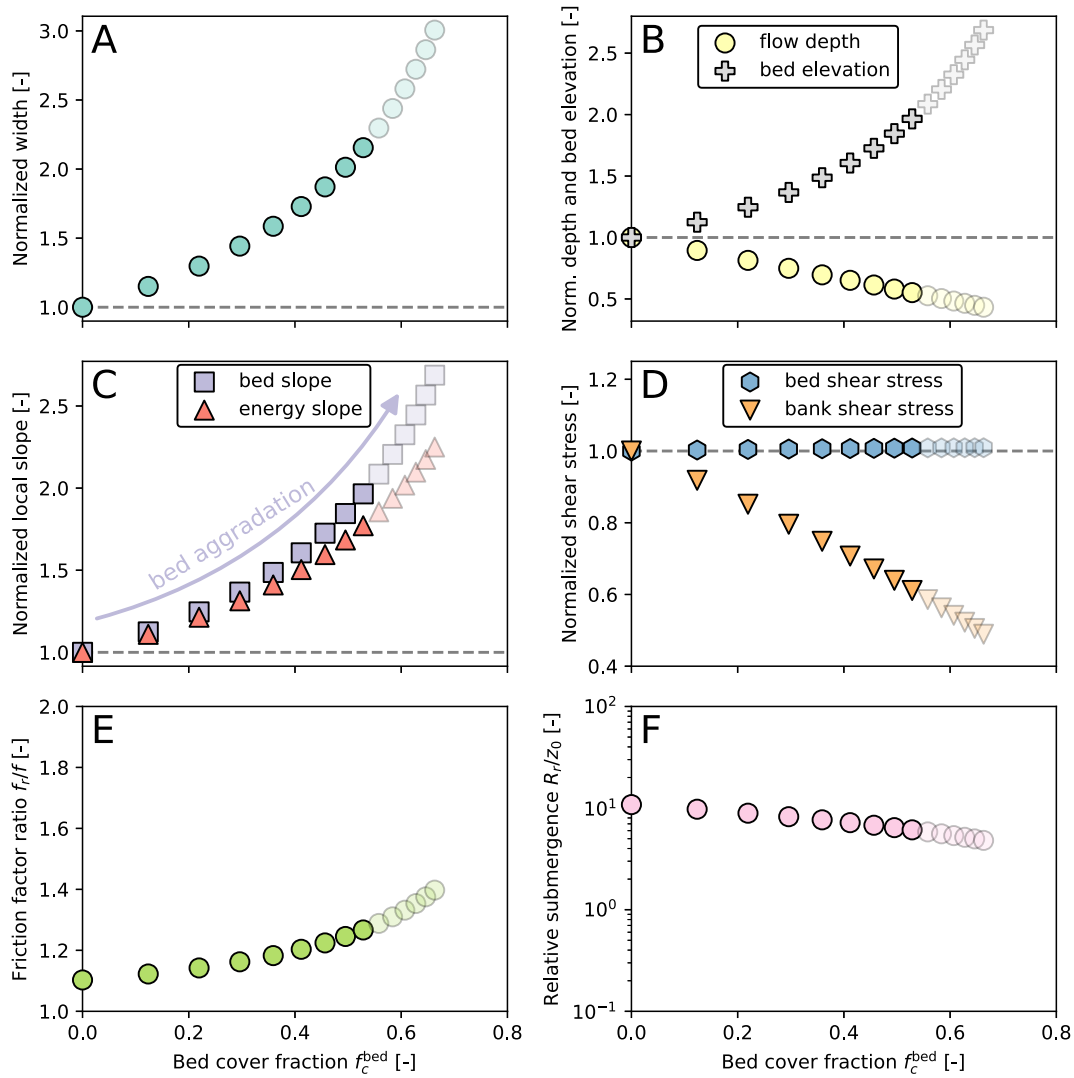

Figure 5. Influence of bed cover on equilibrium channel width (a), flow depth and bed elevation (b), local bed and energy slope (c), bed and bank shear stress (d), friction factor (e), and relative submergence (f) with all other parameters held constant. In (a–d), quantities are normalized to their values in the no-bed-cover end-member $(f_c^{bed} = 0)$. Gray dashed lines show values of 1. The roughness length z_0 is set to 0.1 m for all simulations in this figure to show the effects of cover in a relatively rough flow; in nature z_0 and f_c^{bed} might co-vary. Translucent points represent equilibrium values that the model would achieve in the absence of overbank flow and resulting channel filling. *X*-axis values reflect bed cover at equilibrium.

with bank cover fraction as the channel narrows. The friction factor ratio decreases slightly (Figure 5e) and relative submergence increases slightly (Figure 5f) as channel narrowing deepens the flow while z_0 remains fixed.

3.1.3. Model Sensitivity to Erosion and Deposition Parameters

To test sensitivity of equilibrium channel geometry to the relative efficiency of bed versus bank erosion (k^*_{ero}) and deposition (k^*_{dep}), we run 400 simulations on a 20 × 20 grid defined by $0.1 \leq k^*_{ero} \leq 5$ and $10 \leq k^*_{dep} \leq 100$. These ranges are chosen to illustrate trends in model sensitivity, and result in a wide range of equilibrium geometries.

Equilibrium model outcomes are sensitive to the ratio k^*_{dep}/k^*_{ero} (Figure 7). White dotted lines on Figure 7 illustrate that any given modeled quantity is constant along a line that defines a fixed k^*_{dep}/k^*_{ero} ratio. Deviations from a given k^*_{dep}/k^*_{ero} ratio, by changing either k^*_{ero} or k^*_{dep}, drive reasonably intuitive modeled responses. With all else equal, equilibrium channels become narrower, deeper, and less steep as k^*_{ero} increases and drives preferential

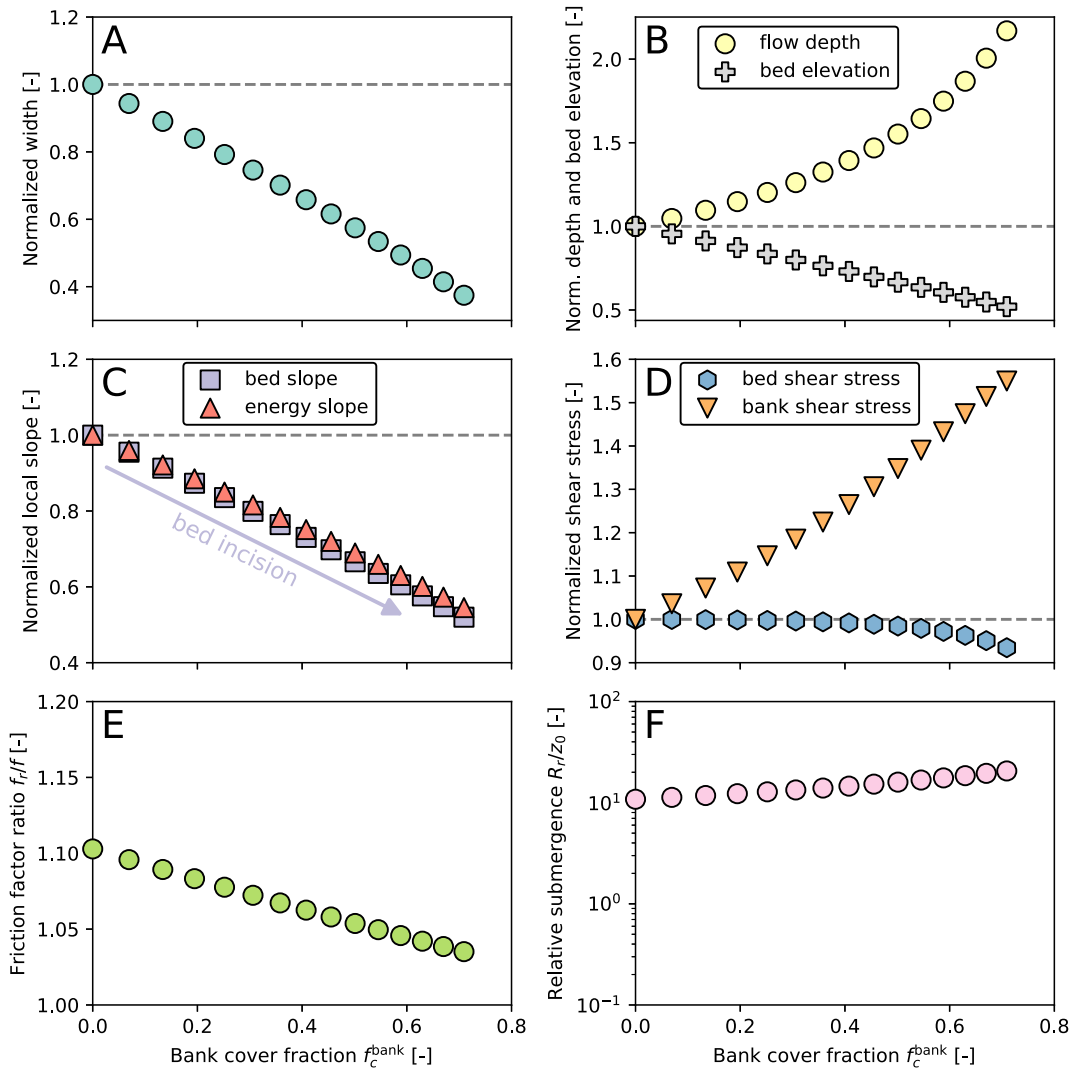

Figure 6. Influence of bank cover on equilibrium channel width (a), flow depth and bed elevation (b), local bed and energy slope (c), bed and bank shear stress (d), friction factor (e), and relative submergence (f) with all other parameters held constant. In (a–d), quantities are normalized to their values in the no-bank-cover end-member $\left(f_c^{bank} = 0\right)$. Gray dashed lines show values of 1. The roughness length z_0 is set to 0.1 m for all simulations in this figure to show the effects of cover in a relatively rough flow; in nature z_0 and f_c^{bank} might co-vary. *X*-axis values reflect bank cover at equilibrium.

erosion of the bed relative to the banks (Figures 7a–7c). Deepening and narrowing cause increases in bank shear stress (Figure 7d), decreases in f_r/f (Figure 7e), and increases in relative submergence (Figure 7f). Increases in k^*_{dep} drive channels to widen, shallow, and steepen (Figures 7a–7c) as deposition preferentially occurs on the bed relative to the banks. Widening and shallowing cause reductions in equilibrium bank shear stress (Figure 7d), increases in f_r/f (Figure 7e), and decreases in relative submergence (Figure 7f). The model is more likely to enter the filling regime at low k^*_{ero} and high k^*_{dep} when bed aggradation is most favored (white shaded region in Figure 7). The onset of the filling regime is not fixed at these k^*_{ero} and k^*_{dep} values but changes with modeled conditions. The filling regime region on Figure 7 expands (contracts) when z_0 or Q_s^{in} is greater (smaller). For example, the field application (Section 3.3) shows that a high k^*_{dep}/k^*_{ero} need not cause filling if Q_s^{in} is sufficiently low.

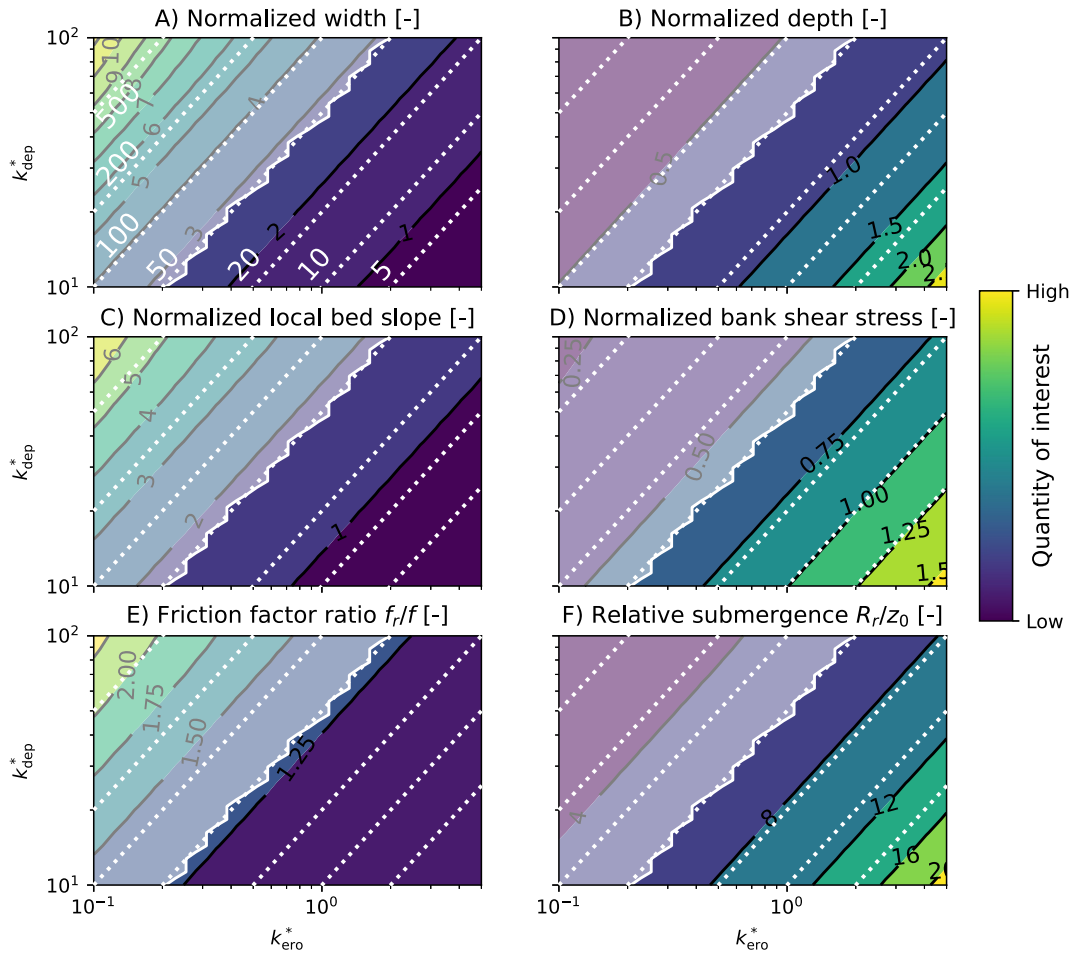

Figure 7. Model sensitivity to the erosion and deposition constants k^*_{ero} and k^*_{dep} with $z_0 = 0.1$ m. Contours are defined by a grid of 400 simulations with logarithmically spaced values along both axes. In (a–d), quantities are normalized to their values in the low-roughness end-member ($z_0 = 0.01$ m). White dotted lines, labeled with white numbers in (a), define constant k^*_{dep}/k^*_{ero} ratios. Translucent white region shows combinations of k^*_{ero} and k^*_{dep} that, under this model parameterization, cause the channel to enter the filling regime.

3.2. Transient Channel Response to Macro-Roughness Increases

We assess the response to macro-roughness increases over three timescales: 0.1% of the longest equilibrium timescale, which corresponds to the months immediately following a change in macro-roughness (Figures 8a, 8d, 8g, 8j, and 8m), 10% of the longest equilibrium timescale, corresponding to the 1–10 years durations over which river restoration monitoring typically occurs (e.g., Maffia et al., 2024) (Figures 8b, 8e, 8h, 8k, and 8n), and 100% of the longest equilibrium timescale, which corresponds to decades to centuries (Figures 8c, 8f, 8i, 8l, and 8o). Timescales are normalized to emphasize comparison among different roughness scenarios rather than exact values. Dashed lines in Figure 8 show trajectories that channels would have experienced had they not entered the filling regime as a result of overbank flow.

Short-term (months) responses to roughening can be nonmonotonic and/or nonlinear as a function of both time and the scale of the roughness perturbation (Figures 8a, 8d, and 8g). For small roughness increases, there are near-immediate, very minor decreases in basal width followed by longer-lasting and greater increases in width over time (Figure 8a). As the roughness perturbation increases (and in the absence of overbank flow that would force channels into the filling regime; dashed lines in Figure 8), channels cease to experience the brief initial narrowing phase and simply increase their width over time. Channels experience abrupt depth increases that scale with the macro-roughness addition (Figure 8d). Most roughness perturbations cause initial reductions in local slope due to

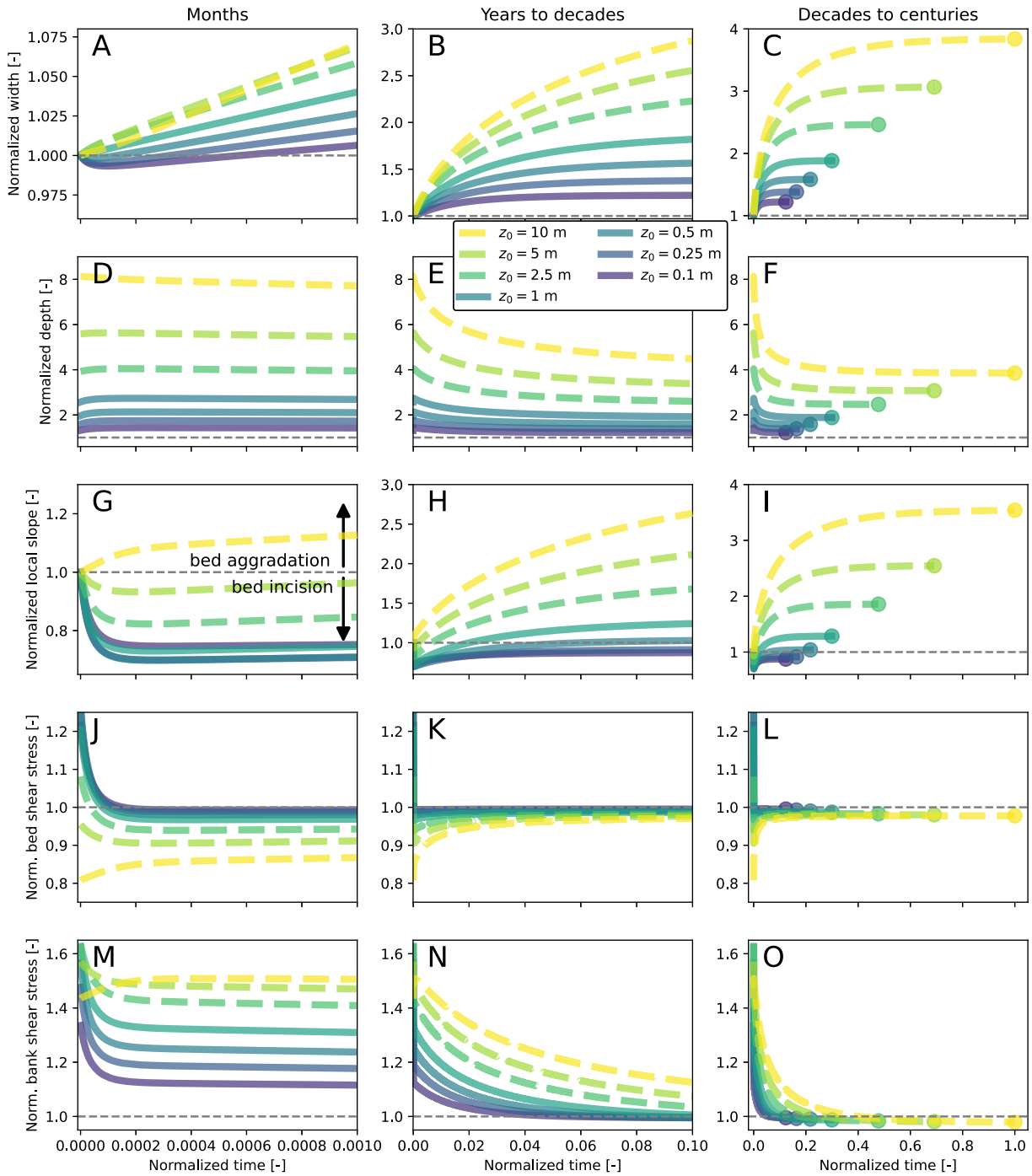

Figure 8. Time series of channel response to an increase in roughness length z_0 from an equilibrium adjusted to $z_0 = 0.01$ m. Each column shows a different time duration. Time is normalized to the longest equilibrium timescale; normalized time is therefore the fraction of the longest equilibrium timescale. Points in the right-hand column show equilibrium adjustment timescales. Dashed lines indicate simulations in which roughness drives flow overbank (see Figure 4); lines show dynamics that would occur in the absence of overbank flow and channel filling.

bed incision followed by slower, longer lasting slope increases driven by bed aggradation (Figure 8g). Under large enough roughness perturbations, there is no initial decline in slope.

Medium- and long-term (years to decades and decades to centuries, respectively) responses to roughness are monotonic with time and with the scale of the roughness perturbation (Figures 8b, 8c, 8e, 8h, 8f, and 8i). After the initial short-term changes in response direction (Figures 8a, 8d, and 8g), channels experience continuous basal

widening, flow shallowing, and bed slope steepening. All three of these responses slow over time as the system approaches equilibrium. Ignoring the potential for overbank flow to shift channels into the filling regime, medium- and long-term channel evolution trajectories are self-similar across the full range of roughness perturbations tested (i.e., solid and dashed lines in Figures 8b, 8c, 8e, 8f, 8h, and 8i have the same characteristic shapes over 0.1%–100% of the maximum equilibrium time scale). Normalized local slopes cross from below 1 (the pre-roughening value) to above 1 over the medium term in some scenarios (Figure 8h).

The morphologic responses described above are coupled to temporal changes in bed and bank shear stress. Bed shear stress undergoes an initial perturbation in response to roughening (Figure 8j), the direction and magnitude of which are controlled by the magnitude of roughening. For increases in roughness where $z_0 \leq 2.5$ m, normalized bed shear stresses increase above 1 before rapidly dropping to values slightly below 1 (Figure 8j) and then slowly recovering toward 1 (Figures 8k and 8l). For greater increases in roughness ($z_0 \geq 5$ m), normalized bed shear stress does not initially exceed 1 (Figure 8j). The greatest roughness value tested ($z_0 = 10$ m) causes the biggest initial drop in normalized bed shear stress followed by a gradual increase toward 1.

Normalized bank shear stress increases above 1 in initial response to roughening (Figure 8m). For all roughness values investigated, normalized bank shear stress spikes before beginning a long decline toward 1 (Figures 8m–8o). The initial spike in bank shear stress for the highest roughness value tested ($z_0 = 10$ m; dashed yellow line) has a different form from the others in that the peak in bank shear stress arrives later and the initial increase is not as great as for lower-roughness experiments (Figure 8m); this delayed increase in bank stress is what allows some lower-roughness experiments to widen more rapidly than the $z_0 = 10$ m channel in the very early phases of response (Figure 8a). The general pattern of an initial rapid increase in normalized bank shear stress followed by a long gradual decline toward on is common to all roughness increases.

Channel response timescales (i.e., time to reach equilibrium; points in Figure 8) vary systematically with the magnitude of the roughness perturbation. The greater the roughness increase, the longer the channel takes to respond, except in the filled regime where the channel is rapidly erased by aggradation (not shown on Figure 8).

3.3. Application to the Field Example

To show how the model might be applied to natural systems, we parameterize the model with field data from the SF Snoqualmie River (Section 2.3.2). We compare modeled versus measured channel width from 2020, 2022, and 2024 to find best-fit values for k^*_{ero} and k^*_{dep} and explore the results of the best-fit model simulations for both lower-roughness (Figures 9a, 9c, 9e, and 9g) and higher-roughness (Figures 9b, 9d, 9f, and 9h) cases.

In the lower-roughness case, best-fit values for k^*_{ero}, the relative efficiency of bed versus bank erosion, and k^*_{dep}, the relative efficiency of bed versus bank deposition, are 0.1 and 102.8, respectively (Figure 9c), for a $k^*_{\text{dep}}/k^*_{\text{ero}}$ ratio of 1,028. In the higher-roughness case, the best-fit k^*_{ero} is 0.12 and the best-fit k^*_{dep} is 59.8 (Figure 9d), for a $k^*_{\text{dep}}/k^*_{\text{ero}}$ ratio of 498. These high $k^*_{\text{dep}}/k^*_{\text{ero}}$ ratios do not drive channel filling (Figures 9g and 9h), likely because Q_s^{in} at the field site is approximately an order of magnitude lower than in our exploratory simulations (Figure 7). The structure of the misfit surface is similar between the two experiments. The vertical band of low misfit illustrates that, in this case, k^*_{ero} has a much narrower range of reasonable values than k^*_{dep} does, and that best-fit $k^*_{\text{dep}}/k^*_{\text{ero}}$ may vary widely without dramatically changing model-data misfit because of the wide range of good-fitting k^*_{dep}.

Running the model with the best-fit values from each optimization and all other parameters as reported in Section 2.3.2 and Table 2, the model achieves parameterizations that allow it to match the observed time series of channel widths (Figures 9e and 9f). There are two notable increases in modeled width: one in the winter of 2019–2020 and one in the winter of 2021–2022. These pulses correspond to groups of high flow events in the discharge time series (Figure 3b).

Comparisons between modeled and observed channel bed elevation reveal that the model, under best-fit parameterizations found solely through comparison between modeled and observed channel width, generally underpredicts channel bed elevation (Figures 9g and 9h). Modeled bed elevations decline very slightly over the study period. Measured bed elevations exhibit no systematic change over time but vary by up to 0.5 m between observations.

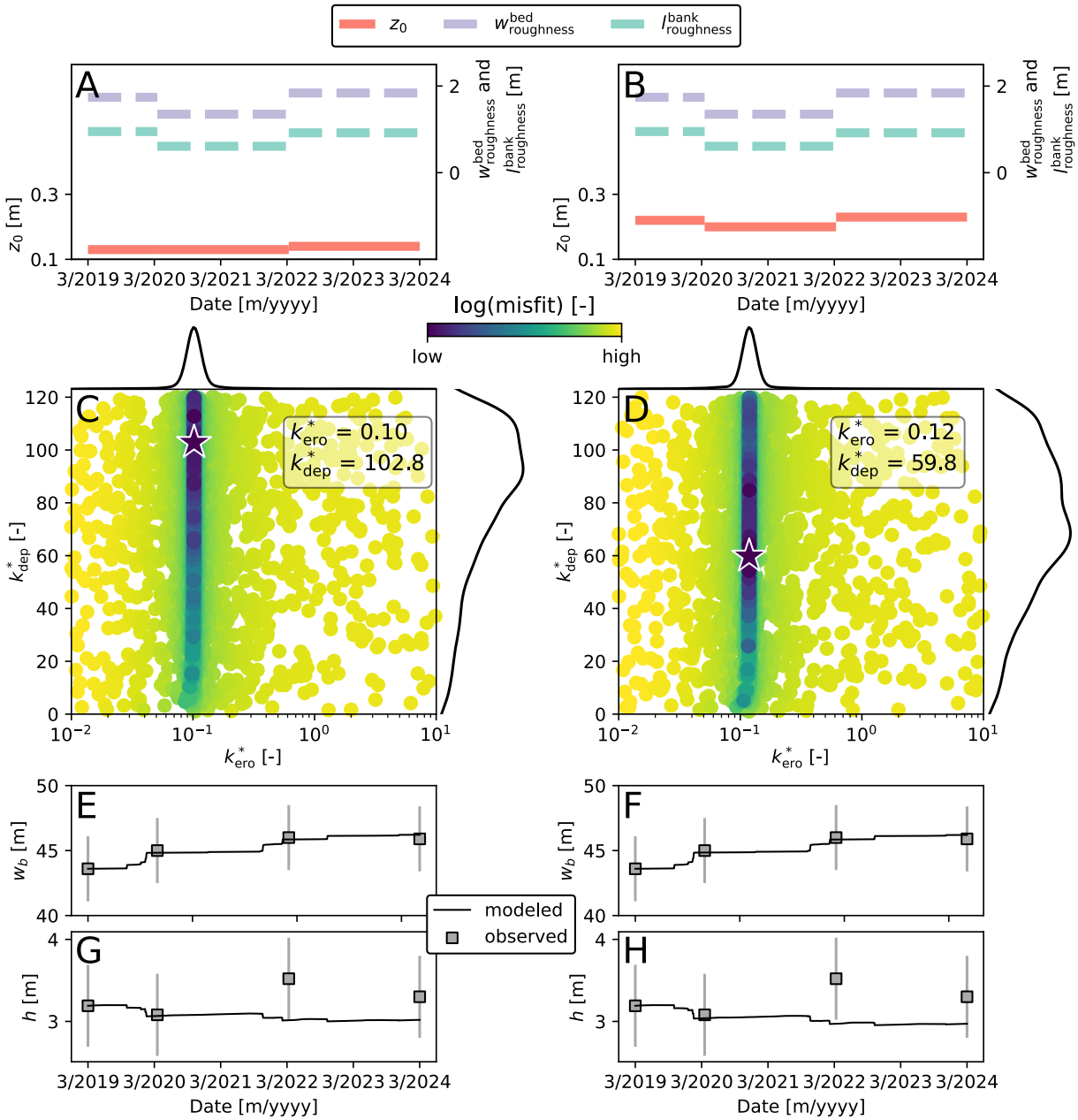

Figure 9. Results from fitting the model to a case study of the SF Snoqualmie River for the low-roughness (a, c, e, g) and high-roughness (b, d, f, h) cases. (a and b) time series of estimates for z_0, $l^{bed}_{roughness}$, and $l^{bank}_{roughness}$ derived from aerial imagery and topobathymetric LiDAR. (c and d) Best-fit values for k^*_{ero} and k^*_{dep} found by minimizing the misfit between modeled and measured channel widths. (e and f) Comparison between modeled and observed channel widths for each best-fit simulation. (g and h) Comparison between modeled and observed channel bed elevation for each best-fit simulation. Error bars for w_b and h are ±2.5 m and ±0.5 m, respectively, reflecting estimated uncertainty arising from measurement of each quantity from LiDAR data.

4. Discussion

4.1. How Does Adding Macro-Roughness Affect Gravel-Bed River Shape and Evolution?

Here we explain the process dynamics by which modeled channels adjust to the addition of macro-roughness. Model results show patterns generally in line with theoretical expectations and regime models, some field evidence, and experimental results for how macro-roughness might affect channel geometry (Eaton & Millar, 2017; Francalanci et al., 2020; Inoue et al., 2025). The diversity of responses to roughening in nature is such that there are also field examples that potentially contradict our model predictions. For example, channels can narrow over

decadal timescales in response to wood loading (Pess et al., 2023), and some streams show little consistent change in response to roughening (Maffia et al., 2024).

4.1.1. Processes Governing Channel Response to Added Roughness

Modeled macro-roughness influences on equilibrium channel geometry vary depending on the magnitude of the roughness forcing as the channel adjusts to maintain constant bank and bed shear stresses (Figure 4d). Modest increases in roughness drive widening-dominated channel responses in which the banks, rather than the bed, experience morphologic change to accommodate roughening (Figure 4a). The initial increase in depth caused by increased flow resistance (Figures 8d–8f) predominantly contributes to widening rather than bed elevation change because, under our stress-partitioning scheme (Flintham & Carling, 1988), bank shear stress is more sensitive to changes in the width/depth ratio for most channel shapes than bed shear stress is. Figure 8m shows that changes in normalized bank shear stress for a given roughness value are greater than changes in bed shear stress. Minor roughening decreases the width/depth ratio, which initially increases the bank shear stress relatively more than it does the bed shear stress. The channel widens to the point at which the bank and bed shear stresses are the same as they were without the additional roughness (Figure 4d) while undergoing very minor bed incision and local slope reduction (Figure 4c). Increased channel width compensates for the reductions in transport capacity imposed by increased macro-roughness and enables sediment to be transported out of the reach at the rate at which it is supplied (Figure 4). The widening response is consistent with field and experimental evidence in cases where in-channel bars are the primary source of macro-roughness (Inoue et al., 2025).

Greater increases in roughness drive a coupled widening and steepening response (Figure 4) due to differential effects of roughening on bed and bank shear stresses caused by increased flow depth and reduced energy slope. Reductions in energy slope would reduce both bed and bank shear stress, but increases in flow depth (Figures 8d–8f) preferentially increase the proportion of shear stress taken up by the banks. Significant roughening therefore causes reduced (after a brief spike for lower roughness values that is accommodated by bed incision; Figure 8g) bed shear stress (Figure 8j) coupled with increased bank shear stress (Figure 8m). The combination of reduced bed stress and increased bank stress drives widening that reduces bank shear stress over time and aggradation that increases bed shear stress over time until both stresses return to baseline values (Figures 8k, 8l, 8n, and 8o). Both a wider channel and increased local slope (via bed aggradation) are required to enable equilibrium sediment transport conditions in the presence of roughness that meaningfully reduces the effective energy slope through increased flow resistance. Aggradation-driven steepening in response to roughening is consistent with some field observations (Addy et al., 2025).

The widening-dominated and widening/steepening regimes are observed when flow cannot go overbank. This case is not as unrealistic as it might seem. Confined channels—those located in deep, narrow valleys—do not experience a cap on flow depth as flows go above bankfull because the floodplain may only be slightly wider than the channel. Channels that have experienced direct (e.g., dredging or levee construction) or indirect (e.g., land-use/land-cover change) human impacts could be sufficiently disconnected from their floodplain that they rarely or never send flow overbank (Simon, 1989). For example, Knox et al. (2022) identify the Mississippi River basin as a hotspot of channels that are disconnected from their floodplains due to levee construction. Deeply incised channels are often targets for restoration, including using methods that increase macro-roughness (Wheaton et al., 2019).

When roughening is sufficient to immediately drive flow overbank, there is no equilibrium channel geometry in the model and the channel fills with sediment. This occurs because the channel aggrades faster than it can widen. The loss of flow overbank prevents flow deepening and therefore eliminates the positive dependence of bank shear stress on roughness. With some flow going overbank there is no mechanism for bank stress to undergo an initial increase that would widen the channel, and bed stress is low enough to allow aggradation. Without the ability to widen while aggrading, the channel progressively loses water conveyance capacity due to bed aggradation and sends more flow overbank. Conceptually, the filled regime represents the kind of channel infilling that might contribute to avulsion (Brummer et al., 2006), and is plausible in rivers with floodplains that can store most or all overbank flow. However, the dominance of the filling regime at all very high roughness conditions is likely due to simplifying model assumptions (especially the lack of any contribution by overbank flow to erosive stresses) and so is better treated as a conceptual end-member than a probable outcome.

Our experiments assessing time-evolving river response to a step increase in roughness suggest that morphologic responses vary considerably depending on the roughness forcing and the time since the step change in roughness. The complexity exhibited by modeled trajectories is important because it implies that some morphologic responses to roughening may be non-monotonic functions of forcing magnitude and/or time. Even our simple experiments with steady water discharge and sediment supply suggest that inferred direction and magnitude of channel adjustment can vary based on (a) the magnitude of the macro-roughness change and (b) when, relative to the timing of changes in macro-roughness, measurements of channel response are made. For example, Figures 8g and 8h show that slope trajectories can transition from below to above their pre-roughening value over time. One common issue with field studies of channel response to roughening is that monitoring can be done frequently (e.g., Flannery et al., 2017) or can cover a long time period (e.g., Pess et al., 2023), but typically not both. Modeled response trajectories might help elucidate the relative impacts of sub-annual and decadal changes and help distinguish ephemeral from persistent responses to roughening.

4.1.2. Processes Governing Channel Response to Added Bed or Bank Cover

Macro-roughness elements influence channel form not only by imposing hydraulic roughness but also by shielding the bed and/or banks from erosive stresses. Increased bed cover requires channel widening and steepening to enable sediment transport out of the reach at the rate of supply (Figure 5). This results in equilibrium bank stress that declines with increases in bed cover because stress partitioning depends primarily on the width/depth ratio, so bank stress declines in wider channels. Increased bank cover causes narrowing and reductions in local slope because the bed provides a more readily available sediment source than the banks do, so the channel narrows and incises to achieve an equilibrium form (Figure 6). Equilibrium bank shear stress increases as the channel narrows.

It is interesting that bank shear stress, rather than bed shear stress, is the quantity that responds to both bed cover (Figure 5) and bank cover (Figure 6) while bed shear stress stays mostly constant. This occurs because in the Flintham and Carling (1988) stress partitioning approach, at width/depth ratios realistic for gravel-bed rivers, bed stress does not vary much with width/depth ratio while bank stress does. This makes bank stress the more sensitive variable to changes in anything that affects the flow geometry and channel shape (roughness, bed cover, bank cover, etc.).

The effects of cover are more complex in nature than in our analysis because bed and bank cover vary over time, co-vary with each other, and co-vary with z_0. Our case study shows an example of this: because our calculation method for z_0 depends explicitly on the area of the bed covered by wood, bed cover and z_0 are more closely tied to one another than they are to bank cover (Figures 9a and 9b). This need not always be the case, and might vary based on the source of macro-roughness. Some river management interventions, for example, increase macro-roughness while purposefully and preferentially shielding the banks (Addy & Wilkinson, 2016).

4.2. Macro-Roughness Effects in Modeled Versus Real Rivers

Our model underestimates the complexity of potential channel responses to added macro-roughness because it contains major simplifications both in terms of model structure and process representations.

The reach-averaged geomorphic model with width- and depth-averaged hydraulics neglects spatial variations in flow velocity and shear stress due to nonuniform flow, as well as longitudinal and cross-stream variability in erosion and deposition rates. The model is therefore best thought of as representing a reach with elevated roughness values rather than a single logjam, boulder, or in-stream structure. Results show general consistency, in terms of roughness-driven modification of reach-averaged friction factors, with ranges from field- and flume-based studies (Figure 4e) (Shields & Gippel, 1995; Wilcox & Wohl, 2006; R. Ferguson, 2007; Follett & Wohl, 2024). The model cannot, however, develop high-velocity near-bank flow driven by the presence of roughness elements (e.g., Zhang et al., 2019; Zhang et al., 2020) or flow structures generated by channel curvature (Wu et al., 2005). These limitations are likely to make themselves felt most strongly at low relative submergence conditions $\left(R_r/z_0 < 10^{-1}\right)$. Nor can the reach-averaged model represent localized erosion or deposition associated with roughness elements (e.g., Addy et al., 2025; Papanicolaou & Tsakiris, 2017). The binary nature of bed and bank cover in our model, in which any given length of the bed/bank is either covered or not covered, may best apply to boulder-mantled beds or those covered by large, dense accumulations of wood. Progress on how different types and arrangements of macro-roughness do or do not protect the channel margin from hydraulic stresses

(e.g., Zhang et al., 2019) might improve our modeling approach. Our method for incorporating macro-roughness effects on bedload transport relies heavily on studies in steep mountain streams (e.g., E. Yager et al., 2007; Schneider et al., 2016) and could be improved by future work on lower-gradient gravel-bed rivers with significant roughness.

The model uses only a simplistic treatment of channel bank erosion processes, assuming that any flow that can transport bedload has the potential to erode the banks if the bank sediment mass balance allows. Although this assumption is reasonable in a long-term average sense (Darby et al., 2010; Nanson & Hickin, 1986) because of the connection between bed mobilization and bank toe undermining, it is a crude abstraction of bank erosion processes. Bank erosion is a stochastic process influenced by vegetation that might stabilize banks (Simon & Collison, 2002), fluvial or seepage-driven erosion that undercuts bank toes (Cancienne et al., 2008), soil saturation that primes banks for mass failure (Rinaldi & Nardi, 2013), and flow sequencing and magnitude (Davidson & Eaton, 2018). Incorporating these processes would likely not affect the general trajectories we present, but might superimpose phases of both widening and narrowing onto those trajectories and change predicted channel response timescales. See Z. Li et al. (2025) for a review of more detailed bank erosion modeling approaches.

To preserve the generality of our approach to different types of roughness elements (wood, boulders, restoration structures, etc.), we neglect processes that might change the roughness length scale and bed/bank cover over time. In natural rivers, there exist two-way feedbacks between channel morphology and roughness. For example, channels can self-adjust roughness through changes to the grain size distribution (e.g., Langendoen & Alonso, 2008) or the development of bedforms (Inoue et al., 2025). In mountain rivers, bed incision can trigger delivery of large boulders by undercutting adjacent hillslopes (Golly et al., 2017; Shobe et al., 2016). Wood loads in rivers vary due to spatiotemporal changes in wood recruitment, which can be driven by channel widening, avulsion, or lateral migration (e.g., Comiti et al., 2016), as well as changes in wood transport, which also depends on channel geometry (Ruiz-Villanueva et al., 2016). In-stream structures commonly installed as part of low-tech, process-based restoration efforts are intentionally impermanent and may persist for less time than our modeling suggests might be required for channel form to equilibrate to their presence (Shahverdian et al., 2019).

There is considerable uncertainty in how this model, or others using similar process representations, should be parameterized with field data. There is no standard method for calculating the roughness length scale z_0, the extent to which such a calculation should focus on grain-scale versus bedform-scale roughness is unclear (R. I. Ferguson et al., 2024), and any single length scale may be insufficient to describe roughness variability in natural rivers (Houseago et al., 2025). The standard deviation of bed elevation has recently been suggested as the best-performing single descriptor of roughness when applying the VPE (Chen et al., 2025). We used an ad hoc methodology that is not inconsistent with current guidance (R. I. Ferguson et al., 2024; Chen et al., 2025), but expect that ongoing work may reveal improved methods for incorporating field data into simplified models.

The constants that proportion erosion and deposition between the bed and banks (k^*_{ero} and k^*_{dep}, respectively) control modeled channel response to roughening (Figure 7); end-member values can cause channels to attain equilibrium forms that are improbable. Equilibrium channel morphology varies monotonically as a function of the $k^*_{\mathrm{dep}}/k^*_{\mathrm{ero}}$ ratio, yielding a wide range of channel morphologies and indicating that it would be important to estimate $k^*_{\mathrm{dep}}/k^*_{\mathrm{ero}}$ at minimum for any field application. Reasonable ranges for the $k^*_{\mathrm{dep}}/k^*_{\mathrm{ero}}$ ratio are likely site-dependent as shown by the convergence on values in the field application (Figure 9) that, in exploratory simulations with greater Q_s^{in}, result in channel filling (Figure 7). $k^*_{\mathrm{dep}}/k^*_{\mathrm{ero}}$ ratios might be interpretable from knowledge of sediment and channel properties. For example, preferential exposure of bedrock, coarse sediment, and/or very cohesive sediment in the bed (banks) might increase (reduce) $k^*_{\mathrm{dep}}/k^*_{\mathrm{ero}}$. Values may also vary over time, if for example, bank stratigraphy of varying erodibility is exposed as a channel incises. For investigations focused on transient behavior, including our field example, the individual values of k^*_{ero} and k^*_{dep} might also matter because the system may be net-erosional or net-depositional. Rate constants like these are difficult to infer for natural systems (e.g., Barnhart et al., 2020b); k^*_{ero} and k^*_{dep} might best be inferred inversely by using the model to match time series of observed channel morphology as we do in our field case study (Figure 9).

Our case study of the SF Snoqualmie River shows how the model can potentially be parameterized to represent a natural system. Given the ability to search for best-fit erosion and deposition constants, a parameterization can be found that is consistent with observations. Reach-averaged roughness variations and geomorphic change

observed in the SF Snoqualmie over the study period are minor relative to the uncertainties on our DEM-based measurements, making our case study better understood as an example of how to parameterize the model than a demonstration of its ability to capture the dynamics of real systems. Other data such as rating curve records (e.g., Pfeiffer et al., 2019) could improve measurement uncertainty and therefore ability to assess model behavior. Future comparison against channels with more dramatic changes in roughness and morphology might better illustrate model capabilities and limitations. Misfit in our case study is very sensitive to the value of the erosion constant k^*_{ero}, indicating that the value of k^*_{ero} is an important control on channel-width change in this system (Figures 9c and 9d). Misfit is much less sensitive to k^*_{dep}. This difference likely arises from a combination of net widening over the study period and the misfit function's exclusive dependence on width. The relative importance of k^*_{ero} and k^*_{dep} might be reversed in rivers experiencing, for example, transient channel narrowing.

4.3. Implications for River Restoration

This paper is motivated in part by the apparent necessity of adding macro-roughness elements like wood and boulders to achieve river restoration goals such as facilitating channel-floodplain connectivity, side channel formation and maintenance, and bed aggradation (Addy et al., 2025; Beechie et al., 2010; Hall et al., 2018; Polvi et al., 2014; Wheaton et al., 2019). Many restoration efforts are attempting to return to rivers roughness that was lost due to logging, in-channel wood removal, and channel modification to enable timber floating (Polvi et al., 2014; Wohl, 2014). Especially in novel riverine ecosystems created by large-scale disturbance (e.g., stand-killing wildfire) in the context of climate change, morphodynamic response can be conditional on macro-roughness (Wohl et al., 2024), and models of transient channel response could be useful in conceptualizing the potential adjustment space.

We observe complex responses to roughening that might be of interest to managers planning restoration efforts. For example, channel width and bed elevation have differing responses to minor roughening (increases in width, very slight bed incision) but consistent responses to major roughening (large increases in width and bed elevation). Although widening is a common response to roughening, if it is not coupled with sufficient aggradation, it could lead to expansion of an incised channel rather than re-occupation of the floodplain (Simon, 1989). Models like the one presented here could be used to explore the relative potential for widening versus aggradation in response to restoration interventions—and how those responses depend on other key variables—filling a gap between high-complexity hydraulic models and equilibrium regime models (Eaton & Millar, 2017), especially in data-poor settings.

Any potential use of models in developing expectations for river response to roughening would require managing their manifold simplifications such as, in this case, the lack of roughness change over time, restriction to a single channel with simplified hydraulics, assumption of uniform bed and bank composition, lack of biotic effects and feedbacks as channels evolve, and rate parameters that may prove difficult to connect with natural systems. Use of simplified models like this one would be enhanced by finding complementary lines of evidence, potentially from the outcomes of past restoration efforts, to validate model predictions.

Although this study applies only to single-thread channels, it represents a step toward understanding macro-roughness effects on bifurcated, multi-channel gravel-bed rivers whose dynamics commonly depend on the spatial distribution of macro-roughness (J. D. Phillips, 2012; Marshall & Wohl, 2023). Bifurcations and side channels are increasingly being used even in urban river restoration to drive floodplain reconnection, habitat diversification, and risk reduction (Stefankiv et al., 2019), and macro-roughness represents a key design parameter used to regulate side channel behavior. Expanding this modeling approach to multi-channel systems might enhance understanding of how macro-roughness influences processes of avulsion and side-channel evolution.

5. Conclusions

A wide array of natural processes and human impacts can alter macro-roughness in gravel-bed rivers, potentially influencing water conveyance and flood hazards, the quality of aquatic habitat, and long-term landscape change. We asked how channels respond to abrupt increases in macro-roughness as might occur due to landslide boulder delivery, increases in wood supply, or restoration efforts, both in terms of their equilibrium geometry and transient response trajectories. We developed a reach-averaged model for the evolution of channel geometry over

time in the presence of macro-roughness. We then parameterized the model to approximate a wood-rich reach of the SF Snoqualmie River.

Equilibrium simulations reveal three regimes of behavior as roughness increases: one in which modest macro-roughness is predominantly accommodated via bank erosion and widening, one in which greater roughness is accommodated by coeval widening and aggradation/steepening, and one in which overbank flow triggers rapid aggradation that fills the channel. Equilibrium channel morphologies are not always monotonic functions of roughness, but depend on how roughness affects bed and bank shear stress partitioning. Time series of responses to roughening show that the direction, magnitude, and timing of roughness-driven changes to channel morphology vary as a function of the roughness forcing and of time. The field application suggests that although the model abstracts natural processes in many ways, it can achieve parameterizations under which it evolves similarly to a natural gravel-bed river with macro-roughness elements.

Gravel-bed river responses to roughening can be complex and contingent on factors ranging from the relative erodibility of the bed and banks to the discharge distribution to the pre-existing channel geometry. Insights from simplified, process-based modeling may elucidate the mechanisms driving channel response to macro-roughness changes that arise both naturally and through human intervention. Understanding derived from this and other models might help envision potential outcomes of restoration efforts across diverse geomorphic settings and aid in planning post-restoration monitoring programs.

Appendix A: Derivation of Equation 7

Here we show the algebra involved in obtaining Equation 7 by combining Equations 2–6. Beginning with flow continuity (Equation 3):

$$Q = A_r U_r = \left(w_b + \frac{d_r}{\tan\theta}\right) d_r \sqrt{\frac{8 g R_r S_r}{f_r}}, \tag{A1}$$

we use the Variable-Power Equation (Equation 4):

$$\sqrt{\frac{8}{f_r}} = \frac{a_1 a_2 (R_r/z_0)}{\sqrt{a_1^2 + a_2^2 (R_r/z_0)^{5/3}}}. \tag{A2}$$

to substitute for $\sqrt{\frac{8}{f_r}}$ which yields:

$$Q = A_r U_r = \left(w_b + \frac{d_r}{\tan\theta}\right) d_r \frac{a_1 a_2 (R_r/z_0)}{\sqrt{a_1^2 + a_2^2 (R_r/z_0)^{5/3}}} \sqrt{g R_r S_r}. \tag{A3}$$

We then use the reduced energy slope equation (Equation 5):

$$S_r = S\left(\sqrt{\frac{f}{f_r}}\right)^e \tag{A4}$$

to substitute for S_r and obtain:

$$Q = A_r U_r = \left(w_b + \frac{d_r}{\tan\theta}\right) d_r \frac{a_1 a_2 (R_r/z_0)}{\sqrt{a_1^2 + a_2^2 (R_r/z_0)^{5/3}}} \sqrt{g R_r S\left(\sqrt{\frac{f}{f_r}}\right)^e}. \tag{A5}$$

We then derive an expression to substitute for $\sqrt{\frac{f}{f_r}}$:

$$\sqrt{\frac{f}{f_r}} = \frac{\sqrt{\frac{8}{f_r}}}{\sqrt{\frac{8}{f}}}. \tag{A6}$$

Equation A2 substitutes for $\sqrt{\frac{8}{f_r}}$ and the Manning-Strickler equation (Equation 6):

$$\sqrt{\frac{8}{f}} = a_1(R_r/z_0)^{1/6} \tag{A7}$$

substitutes for $\sqrt{\frac{8}{f}}$, yielding:

$$\sqrt{\frac{f}{f_r}} = \frac{\sqrt{\frac{8}{f_r}}}{\sqrt{\frac{8}{f}}} = \frac{\frac{a_1 a_2 (R_r/z_0)}{\sqrt{a_1^2 + a_2^2 (R_r/z_0)^{5/3}}}}{a_1(R_r/z_0)^{1/6}} = \frac{a_2(R_r/z_0)^{5/6}}{\sqrt{a_1^2 + a_2^2(R_r/z_0)^{5/3}}}. \tag{A8}$$

We can then substitute Equation A8 into Equation A5 to get:

$$Q = A_r U_r = \left(w_b + \frac{d_r}{\tan\theta}\right) d_r \frac{a_1 a_2 (R_r/z_0)}{\sqrt{a_1^2 + a_2^2(R_r/z_0)^{5/3}}} \sqrt{gR_r S \left(\frac{a_2(R_r/z_0)^{5/6}}{\sqrt{a_1^2 + a_2^2(R_r/z_0)^{5/3}}}\right)^e}. \tag{A9}$$

Finally, we can use the geometric relationship between hydraulic radius and depth (Equation 2):

$$R_r = \frac{\left(w_b + \frac{d_r}{\tan\theta}\right) d_r}{w_b + 2\frac{d_r}{\sin\theta}}, \tag{A10}$$

to yield an equation that can be solved iteratively for depth given a known discharge (Equation 7):

$$Q = \left(w_b + \frac{d_r}{\tan\theta}\right) d_r \frac{a_1 a_2 \left(\frac{\left(w_b + \frac{d_r}{\tan\theta}\right) d_r}{w_b + 2\frac{d_r}{\sin\theta}} / z_0\right)}{\sqrt{a_1^2 + a_2^2 \left(\frac{\left(w_b + \frac{d_r}{\tan\theta}\right) d_r}{w_b + 2\frac{d_r}{\sin\theta}} / z_0\right)^{5/3}}} \sqrt{g \frac{\left(w_b + \frac{d_r}{\tan\theta}\right) d_r}{w_b + 2\frac{d_r}{\sin\theta}} S \left(\frac{a_2 \left(\frac{\left(w_b + \frac{d_r}{\tan\theta}\right) d_r}{w_b + 2\frac{d_r}{\sin\theta}} / z_0\right)^{5/6}}{\sqrt{a_1^2 + a_2^2 \left(\frac{\left(w_b + \frac{d_r}{\tan\theta}\right) d_r}{w_b + 2\frac{d_r}{\sin\theta}} / z_0\right)^{5/3}}}\right)^e}. \tag{A11}$$

Notation

w_b	Basal channel width [L]
d_r	Flow depth [L]
θ	Bank angle [degrees]
d_c	Channel depth [L]
h_{fp}	Floodplain elevation [L]
h	Channel bed elevation [L]
h_{bl}	Baselevel elevation [L]
S	Local channel bed slope [−]
L	Reach length [L]

τ_r	Effective boundary shear stress [$ML^{-1}\ T^{-2}$]
ρ_w	Density of water [ML^{-3}]
g	Acceleration due to gravity [LT^{-2}]
R_r	Hydraulic radius [L]
S_r	Effective energy slope [−]
Q	Water discharge [L^3T^{-1}]
A_r	Flow cross-section area [L^2]
U_r	Reach-averaged flow velocity [LT^{-1}]
f	Friction factor in the absence of macro-roughness [−]
f_r	Friction factor [−]
e	Energy slope exponent [−]
a_1	Flow resistance relation constant [−]
a_2	Flow resistance relation constant [−]
z_0	Roughness length scale [L]
Q_s^{in}	Volumetric sediment flux into the reach [$L^3\ T^{-1}$]
Q_s^{out}	Volumetric sediment flux out of the reach [$L^3\ T^{-1}$]
w_r	Channel width at the water surface [L]
f_c^{tot}	Fraction of the channel boundary shielded by roughness elements [−]
ρ_s	Density of sediment grains [ML^{-3}]
D_{50}	Median bed grain size [L]
τ_{bank}	Bank shear stress [$ML^{-1}\ T^{-2}$]
τ_{bed}	Bed shear stress [$ML^{-1}\ T^{-2}$]
F_w	Proportion of shear force exerted on the banks [−]
$\frac{\partial h_{\text{bed}}}{\partial t}$	Surface-normal rate of bed surface change [LT^{-1}]
$\frac{\partial h_{\text{bank}}}{\partial t}$	Surface-normal rate of bank surface change [LT^{-1}]
l_{bank}	Cross-stream length of one bank [L]
D_{bed}	Surface-normal rate of bed deposition [LT^{-1}]
E_{bed}	Surface-normal rate of bed erosion [LT^{-1}]
D_{bank}	Surface-normal rate of bank deposition [LT^{-1}]
E_{bank}	Surface-normal rate of bank erosion [LT^{-1}]
ϕ	Porosity of bed and bank material [−]
k_{dep}^*	Relative efficiency of bed to bank deposition [−]
k_{ero}^*	Relative efficiency of bed to bank erosion [−]
a	Shear stress exponent [−]
$w_{\text{roughness}}^{\text{bed}}$	Width of the channel bed shielded by roughness elements [L]
$l_{\text{roughness}}^{\text{bank}}$	Cross-stream length of one channel bank shielded by roughness elements [L]

f_c^{bank}	Fraction of the cross-stream bank length shielded by roughness elements [−]
f_c^{bed}	Fraction of the cross-stream bed width shielded by roughness elements [−]
Δt	Model timestep [T]
p_b	Case study: Proportion of sediment traveling as bedload [−]
k	Case study: Sediment rating coefficient [TL^{-3}]
m	Case study: Sediment rating exponent [−]
σ_z^{base}	Case study: Bed roughness length in areas without wood [L]
σ_z^{wood}	Case study: Bed roughness length in areas with wood [L]
A_{base}	Case study: Area of the bed without wood [L^2]
A_{wood}	Case study: Area of the bed covered by wood [L^2]
A_{tot}	Case study: Total bed area [L^2]
$\boldsymbol{\mu}$	Case study: Model-data misfit [−]
δ	Case study: Uncertainty on width measurements [L]

Conflict of Interest

The authors declare no conflicts of interest relevant to this study.

Availability Statement

Model code, driver scripts, and inputs to reproduce all simulations in this paper are permanently and publicly available at https://doi.org/10.5281/zenodo.20709059 (Shobe, 2026).

Acknowledgments
This work was supported by the U.S. Department of Agriculture, Forest Service and by NSF award EAR-2220337 to CMS. The findings and conclusions in this publication are those of the authors and should not be construed to represent any official USDA or U.S. Government determination or policy. Thanks go to Rachel Glade, Katherine Lininger, and Elowyn Yager for helpful discussions. Shelby Ahrendt, Gary Parker, Elowyn Yager, and Associate Editor Peter Nelson provided constructive reviews.

References

Abramian, A., Devauchelle, O., & Lajeunesse, E. (2020). Laboratory rivers adjust their shape to sediment transport. *Physical Review E*, *102*(5), 053101. https://doi.org/10.1103/physreve.102.053101

Addy, S., & Wilkinson, M. (2016). An assessment of engineered log jam structures in response to a flood event in an upland gravel-bed river. *Earth Surface Processes and Landforms*, *41*(12), 1658–1670. https://doi.org/10.1002/esp.3936

Addy, S., Wilkinson, M., & Quinn, P. (2025). The hydro-geomorphic effects of wooden leaky barriers in a steep headwater stream. *Earth Surface Processes and Landforms*, *50*(6), e70079. https://doi.org/10.1002/esp.70079

Ahrendt, S., Horner-Devine, A. R., Collins, B. D., Morgan, J. A., & Istanbulluoglu, E. (2022). Channel conveyance variability can influence flood risk as much as streamflow variability in western washington state. *Water Resources Research*, *58*(6), e2021WR031890. https://doi.org/10.1029/2021wr031890

Ahrendt, S. M., Mirus, B. B., LaHusen, S. R., & Perkins, J. P. (2025). Dynamic feedbacks between river meandering and landsliding in northwestern Washington glacial terraces. *Journal of Geophysical Research: Earth Surface*, *130*(8), e2024JF008249. https://doi.org/10.1029/2024JF008249

Alzabari, F., Wilson, C. A., & Ouro, P. (2024). Hydrodynamics of in-stream leaky barriers for natural flood management. *Water Resources Research*, *60*(12), e2024WR038117. https://doi.org/10.1029/2024wr038117

Barnhart, K. R., Tucker, G. E., Doty, S. G., Shobe, C. M., Glade, R. C., Rossi, M. W., & Hill, M. C. (2020a). Inverting topography for landscape evolution model process representation: 2. Calibration and validation. *Journal of Geophysical Research: Earth Surface*, *125*(7), e2018JF004963. https://doi.org/10.1029/2018JF004963

Barnhart, K. R., Tucker, G. E., Doty, S. G., Shobe, C. M., Glade, R. C., Rossi, M. W., & Hill, M. C. (2020b). Inverting topography for landscape evolution model process representation: 3. Determining parameter ranges for select mature geomorphic transport laws and connecting changes in fluvial erodibility to changes in climate. *Journal of Geophysical Research: Earth Surface*, *125*(7), e2019JF005287. https://doi.org/10.1029/2019jf005287

Bathurst, J. C. (1978). Flow resistance of large-scale roughness. *Journal of the Hydraulics Division*, *104*(12), 1587–1603. https://doi.org/10.1061/jyceaj.0005114

Beechie, T. J., Sear, D. A., Olden, J. D., Pess, G. R., Buffington, J. M., Moir, H., et al. (2010). Process-based principles for restoring river ecosystems. *BioScience*, *60*(3), 209–222. https://doi.org/10.1525/bio.2010.60.3.7

Blom, A., Arkesteijn, L., Chavarrías, V., & Viparelli, E. (2017). The equilibrium alluvial river under variable flow and its channel-forming discharge. *Journal of Geophysical Research: Earth Surface*, *122*(10), 1924–1948. https://doi.org/10.1002/2017JF004213

Booth, D., Bell, K., & Whipple, K. (1991). *Sediment transport along the south fork and mainstem of the Snoqualmie river*. King County Department of Public Works, Surface Water Management Division.

Brummer, C. J., Abbe, T. B., Sampson, J. R., & Montgomery, D. R. (2006). Influence of vertical channel change associated with wood accumulations on delineating channel migration zones, Washington, USA. *Geomorphology*, *80*(3–4), 295–309. https://doi.org/10.1016/j.geomorph.2006.03.002

Buffington, J. M., & Montgomery, D. R. (2022). Geomorphic classification of rivers: An updated review. In J. (J.) F. Shroder (Ed.), *Treatise on geomorphology* (2nd ed., pp. 1143–1190). Academic Press.

Cancienne, R. M., Fox, G. A., & Simon, A. (2008). Influence of seepage undercutting on the stability of root-reinforced streambanks. *Earth Surface Processes and Landforms: The Journal of the British Geomorphological Research Group*, *33*(11), 1769–1786. https://doi.org/10.1002/esp.1657

Canovaro, F., Paris, E., & Solari, L. (2007). Effects of macro-scale bed roughness geometry on flow resistance. *Water Resources Research*, *43*(10). https://doi.org/10.1029/2006wr005727

Chen, X., Wang, T., Wang, J., Ma, H., Hassan, M. A., & Fu, X. (2025). A unified flow resistance formula for open-channels with natural and engineered submerged obstacles. *Water Resources Research*, *61*(9), e2024WR039242. https://doi.org/10.1029/2024wr039242

Chiari, M., & Rickenmann, D. (2011). Back-calculation of bedload transport in steep channels with a numerical model. *Earth Surface Processes and Landforms*, *36*(6), 805–815. https://doi.org/10.1002/esp.2108

Ciotti, D. C., Mckee, J., Pope, K. L., Kondolf, G. M., & Pollock, M. M. (2021). Design criteria for process-based restoration of fluvial systems. *BioScience*, *71*(8), 831–845. https://doi.org/10.1093/biosci/biab065

Comiti, F., Lucía, A., & Rickenmann, D. (2016). Large wood recruitment and transport during large floods: A review. *Geomorphology*, *269*, 23–39. https://doi.org/10.1016/j.geomorph.2016.06.016

Darby, S. E., Trieu, H. Q., Carling, P. A., Sarkkula, J., Koponen, J., Kummu, M., et al. (2010). A physically based model to predict hydraulic erosion of fine-grained riverbanks: The role of form roughness in limiting erosion. *Journal of Geophysical Research*, *115*(F4). https://doi.org/10.1029/2010jf001708

Davidson, S., & Eaton, B. (2018). Beyond regime: A stochastic model of floods, bank erosion, and channel migration. *Water Resources Research*, *54*(9), 6282–6298. https://doi.org/10.1029/2017wr022059

Davis, J., Lautz, L., Kelleher, C., Vidon, P., Russoniello, C., & Pearce, C. (2021). Evaluating the geomorphic channel response to beaver dam analog installation using unoccupied aerial vehicles. *Earth Surface Processes and Landforms*, *46*(12), 2349–2364. https://doi.org/10.1002/esp.5180

Deal, E. (2022). Flow resistance in very rough channels. *Water Resources Research*, *58*(10), e2021WR031790. https://doi.org/10.1029/2021WR031790

Eaton, B. C., Church, M., & Millar, R. G. (2004). Rational regime model of alluvial channel morphology and response. *Earth Surface Processes and Landforms*, *29*(4), 511–529. https://doi.org/10.1002/esp.1062

Eaton, B. C., MacKenzie, L., Jakob, M., & Weatherly, H. (2017). Assessing erosion hazards due to floods on fans: Physical modeling and application to engineering challenges. *Journal of Hydraulic Engineering*, *143*(8), 04017021. https://doi.org/10.1061/(asce)hy.1943-7900.0001318

Eaton, B. C., & Millar, R. (2017). Predicting gravel bed river response to environmental change: The strengths and limitations of a regime-based approach. *Earth Surface Processes and Landforms*, *42*(6), 994–1008. https://doi.org/10.1002/esp.4058

Ferguson, R. (2007). Flow resistance equations for gravel-and boulder-bed streams. *Water Resources Research*, *43*(5). https://doi.org/10.1029/2006wr005422

Ferguson, R., & Recking, A. (2025). Flow resistance and hydraulic geometry in gravel-and boulder-bed rivers. *Water Resources Research*, *61*(3), e2024WR038852. https://doi.org/10.1029/2024wr038852

Ferguson, R. I., Hardy, R. J., Hodge, R. A., Houseago, R. C., Yager, E. M., & Yamasaki, T. N. (2024). Predicting flow resistance in rough-bed rivers from topographic roughness: Review and open questions. *Earth Surface Processes and Landforms*.

Flannery, J., Stubblefield, A., Fiori, R., & Shea, C. (2017). Observations of channel change from constructed wood jams on a forested gravel-bed stream. *Transactions of the American Fisheries Society*, *146*(1), 181–193. https://doi.org/10.1080/00028487.2016.1235615

Flintham, T., & Carling, P. (1988). Prediction of mean bed and wall boundary shear in uniform and compositely rough channels. In *River regime* (pp. 267–287).

Follett, E., & Wohl, E. (2024). Channel-spanning logjams and reach-scale hydraulic resistance in mountain streams. *Geophysical Research Letters*, *51*(17), e2024GL110126. https://doi.org/10.1029/2024gl110126

Francalanci, S., Lanzoni, S., Solari, L., & Papanicolaou, A. (2020). Equilibrium cross section of river channels with cohesive erodible banks. *Journal of Geophysical Research: Earth Surface*, *125*(1), e2019JF005286. https://doi.org/10.1029/2019jf005286

Fryirs, K. A. (2017). River sensitivity: A lost foundation concept in fluvial geomorphology. *Earth Surface Processes and Landforms*, *42*(1), 55–70. https://doi.org/10.1002/esp.3940

Gabel, V., Tucker, G. E., & Campforts, B. (2024). A mathematical model for bedrock incision in near-threshold gravel-bed rivers. *Earth Surface Processes and Landforms*, *49*(13), 4168–4186. https://doi.org/10.1002/esp.5957

Galia, T., & Poledniková, Z. (2025). Two decades of meander belt morphodynamics: How important is woody vegetation and in-channel large wood? *Catena*, *249*, 108673. https://doi.org/10.1016/j.catena.2024.108673

Gilbert, G. K. (1917). *Hydraulic-mining debris in the sierra Nevada (No. 105)*. US Government Printing Office.

Gippel, C. J., O'Neill, I. C., Finlayson, B. L., & Schnatz, I. (1996). Hydraulic guidelines for the re-introduction and management of large woody debris in lowland rivers. *Regulated Rivers: Research and Management*, *12*(2–3), 223–236. https://doi.org/10.1002/(sici)1099-1646(199603)12:2/3<223::aid-rrr391>3.0.co;2-%23

Golly, A., Turowski, J. M., Badoux, A., & Hovius, N. (2017). Controls and feedbacks in the coupling of mountain channels and hillslopes. *Geology*, *45*(4), 307–310. https://doi.org/10.1130/g38831.1

Gurnell, A. (2014). Plants as river system engineers. *Earth Surface Processes and Landforms*, *39*(1), 4–25. https://doi.org/10.1002/esp.3397

Gurnell, A., Piégay, H., Swanson, F., & Gregory, S. (2002). Large wood and fluvial processes. *Freshwater Biology*, *47*(4), 601–619. https://doi.org/10.1046/j.1365-2427.2002.00916.x

Hall, J. E., Greene, C. M., Stefankiv, O., Anderson, J. H., Timpane-Padgham, B., Beechie, T. J., & Pess, G. R. (2018). Large river habitat complexity and productivity of puget sound chinook salmon. *PLoS One*, *13*(11), e0205127. https://doi.org/10.1371/journal.pone.0205127

Houseago, R., Hodge, R., Asher, B., Ferguson, R., Hackney, C., Hardy, R., et al. (2025). Quantifying bed surface roughness in bedrock and boulder-bed rivers. *Journal of Geophysical Research: Earth Surface*, *130*(5), e2024JF007996. https://doi.org/10.1029/2024jf007996

Inoue, T., Hiramatsu, Y., Johnson, J. P., Dempo, J., & Mishra, J. (2025). Ratio of river channel bar to bank height sets bank erosion rate. *Journal of Geophysical Research: Earth Surface*, *130*(1), e2024JF007965. https://doi.org/10.1029/2024jf007965

Kean, J. W., & Smith, J. D. (2006). Form drag in rivers due to small-scale natural topographic features: 1. regular sequences. *Journal of Geophysical Research*, *111*(F4). https://doi.org/10.1029/2006jf000467

Knox, R., Morrison, R., & Wohl, E. (2022). Identification of artificial levees in the contiguous United States. *Water Resources Research*, *58*(4), e2021WR031308. https://doi.org/10.1029/2021wr031308

Lague, D. (2010). Reduction of long-term bedrock incision efficiency by short-term alluvial cover intermittency. *Journal of Geophysical Research*, *115*(F2). https://doi.org/10.1029/2008jf001210

Langendoen, E. J., & Alonso, C. V. (2008). Modeling the evolution of incised streams: I. model formulation and validation of flow and streambed evolution components. *Journal of Hydraulic Engineering*, *134*(6), 749–762. https://doi.org/10.1061/(asce)0733-9429(2008)134:6(749)

L'Hommedieu, W., Tullos, D., & Jones, J. (2020). Effects of an engineered log jam on spatial variability of the flow field across submergence depths. *River Research and Applications*, *36*(3), 383–397. https://doi.org/10.1002/rra.3555

Li, T., Venditti, J. G., Rennie, C. D., & Nelson, P. A. (2022). Bed and bank stress partitioning in bedrock rivers. *Journal of Geophysical Research: Earth Surface*, *127*(2), e2021JF006360. https://doi.org/10.1029/2021jf006360

Li, Z., Langendoen, E. J., & García, M. H. (2025). Unveiling the stochasticity of bank erosion: A hybrid deterministic and stochastic modeling approach. *Water Resources Research*, *61*(11), e2024WR039336. https://doi.org/10.1029/2024wr039336

Maffia, M. M., Segura, C., Lorion, C. M., Suring, E., & Warren, D. R. (2024). Restoring streams with large wood: An analysis of geomorphic changes 7 years post-restoration in small coastal streams. *Earth Surface Processes and Landforms*.

Marshall, A., & Wohl, E. (2023). The continuum of wood-induced channel bifurcations. *Frontiers in Water*, *5*, 1155623. https://doi.org/10.3389/frwa.2023.1155623

Martín-Vide, J. P., Fael, C. M., Núñez-González, F., Ferrer-Boix, C., Santos, C. A., Prats-Puntí, A., & Chavarrias, V. (2022). A large bridge pier in an alluvial channel: Local scour versus morphological effects and the role of physical models. *Journal of Hydraulic Engineering*, *148*(8), 05022001. https://doi.org/10.1061/(asce)hy.1943-7900.0001993

Meyer-Peter, E., & Müller, R. (1948). Formulas for bed-load transport. In *Proceedings of the 2nd meeting, stockholm* (pp. 39–64).

Millar, R. G. (1999). Grain and form resistance in gravel-bed rivers. *Journal of Hydraulic Research*, *37*(3), 303–312.

Monsalve, A., Yager, E. M., & Schmeeckle, M. W. (2017). Effects of bed forms and large protruding grains on near-bed flow hydraulics in low relative submergence conditions. *Journal of Geophysical Research: Earth Surface*, *122*(10), 1845–1866. https://doi.org/10.1002/2016jf004152

Müller, S., Follett, E., Ouro, P., & Wilson, C. (2022). Influence of channel-spanning engineered logjam structures on channel hydrodynamics. *Water Resources Research*, *58*(12), e2022WR032111. https://doi.org/10.1029/2022wr032111

Nanson, G. C., & Hickin, E. J. (1986). A statistical analysis of bank erosion and channel migration in Western Canada. *Geological Society of America Bulletin*, *97*(4), 497–504. https://doi.org/10.1130/0016-7606(1986)97<497:asaobe>2.0.co;2

Nelson, L. M. (1971). *Sediment transport by streams in the snohomish river basin, Washington: October 1967-june 1969*. US Department of the Interior, Geological Survey, Water Resources Division.

Nitsche, M., Rickenmann, D., Turowski, J. M., Badoux, A., & Kirchner, J. W. (2011). Evaluation of bedload transport predictions using flow resistance equations to account for macro-roughness in steep mountain streams. *Water Resources Research*, *47*(8). https://doi.org/10.1029/2011wr010645

Papanicolaou, A., & Tsakiris, A. G. (2017). Boulder effects on turbulence and bedload transport. *Gravel-Bed Rivers: Processes and Disasters*, 33–72.

Parker, G. (1978). Self-formed straight rivers with equilibrium banks and mobile bed. Part 2. The gravel river. *Journal of Fluid Mechanics*, *89*(1), 127–146. https://doi.org/10.1017/s0022112078002505

Parker, G. (1979). Hydraulic geometry of active gravel rivers. *Journal of the Hydraulics Division*, *105*(9), 1185–1201. https://doi.org/10.1061/jyceaj.0005275

Pearce, C., Vidon, P., Lautz, L., Kelleher, C., & Davis, J. (2021). Short-term impact of beaver dam analogues on streambank erosion and deposition in semi-arid landscapes of the western USA. *River Research and Applications*, *37*(7), 1032–1037. https://doi.org/10.1002/rra.3825

Pess, G. R., McHenry, M. L., Liermann, M. C., Hanson, K. M., & Beechie, T. J. (2023). How does over two decades of active wood reintroduction result in changes to stream channel features and aquatic habitats of a forested river system? *Earth Surface Processes and Landforms*, *48*(4), 817–829. https://doi.org/10.1002/esp.5520

Pfeiffer, A. M., Finnegan, N. J., & Willenbring, J. K. (2017). Sediment supply controls equilibrium channel geometry in gravel rivers. *Proceedings of the National Academy of Sciences*, *114*(13), 3346–3351. https://doi.org/10.1073/pnas.1612907114

Pfeiffer, A. M., Collins, B. D., Anderson, S. W., Montgomery, D. R., & Istanbulluoglu, E. (2019). River bed elevation variability reflects sediment supply, rather than peak flows, in the uplands of Washington state. *Water Resources Research*, *55*(8), 6795–6810. https://doi.org/10.1029/2019wr025394

Phillips, C. B., Masteller, C. C., Blaylock, J., Van Iwaarden, F., & Johnson, J. P. L. (2024). Variability in river width reveals climatic influence on channel geometry. *Geophysical Research Letters*, *51*(23), e2024GL111789. https://doi.org/10.1029/2024gl111789

Phillips, C. B., Masteller, C. C., Slater, L. J., Dunne, K. B., Francalanci, S., Lanzoni, S., et al. (2022). Threshold constraints on the size, shape and stability of alluvial rivers. *Nature Reviews Earth and Environment*, *3*(6), 406–419. https://doi.org/10.1038/s43017-022-00282-z

Phillips, J. D. (2012). Log-jams and avulsions in the San Antonio river Delta, Texas. *Earth Surface Processes and Landforms*, *37*(9), 936–950. https://doi.org/10.1002/esp.3209

Pollock, M. M., Beechie, T. J., Wheaton, J. M., Jordan, C. E., Bouwes, N., Weber, N., & Volk, C. (2014). Using beaver dams to restore incised stream ecosystems. *BioScience*, *64*(4), 279–290. https://doi.org/10.1093/biosci/biu036

Polvi, L. E., Nilsson, C., & Hasselquist, E. M. (2014). Potential and actual geomorphic complexity of restored headwater streams in northern Sweden. *Geomorphology*, *210*, 98–118. https://doi.org/10.1016/j.geomorph.2013.12.025

Powell, D. M. (2014). Flow resistance in gravel-bed rivers: Progress in research. *Earth-Science Reviews*, *136*, 301–338. https://doi.org/10.1016/j.earscirev.2014.06.001

Reid, L. M., & Dunne, T. (1996). Rapid evaluation of sediment budgets. *Catena Reiskirchen*, *29*.

Rice, S. P. (2021). Why so skeptical? The role of animals in fluvial geomorphology. *Wiley Interdisciplinary Reviews: Water*, *8*(6), e1549. https://doi.org/10.1002/wat2.1549

Rickenmann, D. (2012). Alluvial steep channels: Flow resistance, bedload transport prediction, and transition to debris flows. Gravel-Bed Rivers: Processes, Tools. *Environments*, 386–397.

Rickenmann, D., & Recking, A. (2011). Evaluation of flow resistance in gravel-bed rivers through a large field data set. *Water Resources Research*, *47*(7). https://doi.org/10.1029/2010wr009793

Rinaldi, M., & Nardi, L. (2013). Modeling interactions between riverbank hydrology and mass failures. *Journal of Hydrologic Engineering*, *18*(10), 1231–1240. https://doi.org/10.1061/(asce)he.1943-5584.0000716

Ruiz-Villanueva, V., Wyżga, B., Zawiejska, J., Hajdukiewicz, M., & Stoffel, M. (2016). Factors controlling large-wood transport in a mountain river. *Geomorphology*, *272*, 21–31. https://doi.org/10.1016/j.geomorph.2015.04.004

Schalko, I., Schmocker, L., Weitbrecht, V., & Boes, R. M. (2018). Backwater rise due to large wood accumulations. *Journal of Hydraulic Engineering*, *144*(9), 04018056. https://doi.org/10.1061/(asce)hy.1943-7900.0001501

Schneider, J. M., Rickenmann, D., Turowski, J. M., Bunte, K., & Kirchner, J. W. (2015). Applicability of bed load transport models for mixed-size sediments in steep streams considering macro-roughness. *Water Resources Research*, *51*(7), 5260–5283. https://doi.org/10.1002/2014wr016417

Schneider, J. M., Rickenmann, D., Turowski, J. M., Schmid, B., & Kirchner, J. W. (2016). Bed load transport in a very steep mountain stream (r iedbach, s witzerland): Measurement and prediction. *Water Resources Research*, *52*(12), 9522–9541. https://doi.org/10.1002/2016wr019308

Scott, D. N. (2024a). Widespread wood placement and regrading drive lateral connectivity and reworking of the channel and floodplain in a valley bottom reset to stage 0. *Geomorphology*, *446*, 108987. https://doi.org/10.1016/j.geomorph.2023.108987

Scott, D. N. (2024b). Wood jam characteristics influence but do not fully explain wood jam morphologic functions. *Geomorphica*, *1*(1). https://doi.org/10.59236/geomorphica.v1i1.37

Sear, D., Millington, C., Kitts, D., & Jeffries, R. (2010). Logjam controls on channel: Floodplain interactions in wooded catchments and their role in the formation of multi-channel patterns. *Geomorphology*, *116*(3–4), 305–319. https://doi.org/10.1016/j.geomorph.2009.11.022

Shahverdian, S., Wheaton, J., Bennett, S., Bouwes, N., Camp, R., Jordan, C., et al. (2019). Chapter 4 – Mimicking and promoting wood accumulation and beaver dam activity with post-assisted log structures and beaver dam analogues. In *Low-tech process-based restoration of riverscapes: Design manual*. Utah State University Restoration Consortium.

Shields, F. D., Jr., & Gippel, C. J. (1995). Prediction of effects of woody debris removal on flow resistance. *Journal of Hydraulic Engineering*, *121*(4), 341–354. https://doi.org/10.1061/(asce)0733-9429(1995)121:4(341)

Shobe, C. M. (2026). Macro-roughness model code and figure scripts [Software]. *Zenodo*. Retrieved from https://zenodo.org/records/20709059

Shobe, C. M., Bennett, G. L., Tucker, G. E., Roback, K., Miller, S. R., & Roering, J. J. (2021). Boulders as a lithologic control on river and landscape response to tectonic forcing at the mendocino triple junction. *Geological Society of America Bulletin*, *133*(3–4), 647–662. https://doi.org/10.1130/b35385.1

Shobe, C. M., Tucker, G. E., & Anderson, R. S. (2016). Hillslope-derived blocks retard river incision. *Geophysical Research Letters*, *43*(10), 5070–5078. https://doi.org/10.1002/2016gl069262

Simon, A. (1989). A model of channel response in disturbed alluvial channels. *Earth Surface Processes and Landforms*, *14*(1), 11–26. https://doi.org/10.1002/esp.3290140103

Simon, A., & Collison, A. J. (2002). Quantifying the mechanical and hydrologic effects of riparian vegetation on streambank stability. *Earth Surface Processes and Landforms*, *27*(5), 527–546. https://doi.org/10.1002/esp.325

Smith, D. L., Allen, J. B., Eslinger, O., Valenciano, M., Nestler, J., & Goodwin, R. A. (2011). Hydraulic modeling of large roughness elements with computational fluid dynamics for improved realism in stream restoration planning. Stream Restoration in Dynamic Fluvial Systems: Scientific Approaches, Analyses, and Tools, *194*, 115–122.

Stark, C. (2006). A self-regulating model of bedrock river channel geometry. *Geophysical Research Letters*, *33*(4). https://doi.org/10.1029/2005gl023193

Stefankiv, O., Beechie, T. J., Hall, J. E., Pess, G. R., & Timpane-Padgham, B. (2019). Influences of valley form and land use on large river and floodplain habitats in puget sound. *River Research and Applications*, *35*(2), 133–145. https://doi.org/10.1002/rra.3393

Storn, R., & Price, K. (1997). Differential evolution–a simple and efficient heuristic for global optimization over continuous spaces. *Journal of Global Optimization*, *11*(4), 341–359. https://doi.org/10.1023/a:1008202821328

U.S. Geological Survey. (2026). *USGS 12144000 SF Snoqualmie River at North Bend, WA*. USGS Water Data for the Nation. https://doi.org/10.5066/F7P55KJN

Wang, C., Yu, X., & Liang, F. (2017). A review of bridge scour: Mechanism, estimation, monitoring and countermeasures. *Natural Hazards*, *87*(3), 1881–1906. https://doi.org/10.1007/s11069-017-2842-2

Wheaton, J. M., Bennett, S. N., Bouwes, N. W., Maestas, J. D., & Shahverdian, S. M. (2019). *Low-tech process-based restoration of riverscapes: Design manual*. Utah State University Restoration Consortium.

Wickert, A. D., & Schildgen, T. F. (2019). Long-profile evolution of transport-limited gravel-bed rivers. *Earth Surface Dynamics*, *7*(1), 17–43. https://doi.org/10.5194/esurf-7-17-2019

Wieting, C., Friedman, J. M., & Rathburn, S. (2023). River channel response to invasive plant treatment across the american southwest. *Earth Surface Processes and Landforms*, *48*(3), 569–581. https://doi.org/10.1002/esp.5503

Wilcox, A. C., & Wohl, E. E. (2006). Flow resistance dynamics in step-pool stream channels: 1. large woody debris and controls on total resistance. *Water Resources Research*, *42*(5). https://doi.org/10.1029/2005wr004277

Wohl, E. (2013). *Mountain rivers revisited*. John Wiley and Sons.

Wohl, E. (2014). A legacy of absence: Wood removal in us rivers. *Progress in Physical Geography*, *38*(5), 637–663. https://doi.org/10.1177/0309133314548091

Wohl, E. (2015). Legacy effects on sediments in river corridors. *Earth-Science Reviews*, *147*, 30–53. https://doi.org/10.1016/j.earscirev.2015.05.001

Wohl, E., Marshall, A. E., Scamardo, J., White, D., & Morrison, R. R. (2022). Biogeomorphic influences on river corridor resilience to wildfire disturbances in a mountain stream of the southern rockies, USA. *Science of the Total Environment*, *820*, 153321. https://doi.org/10.1016/j.scitotenv.2022.153321

Wohl, E., Rathburn, S., Dunn, S., Iskin, E., Katz, A., Marshall, A., et al. (2024). Geomorphic context in process-based river restoration. *River Research and Applications*, *40*(3), 322–340. https://doi.org/10.1002/rra.4236

Wolstenholme, J. M., Skinner, C. J., Milan, D. J., Thomas, R. E., & Parsons, D. R. (2024). Localised geomorphic response to channel-spanning leaky wooden dams. *EGUsphere*, 1–30. https://doi.org/10.5194/egusphere-2024-3001

Wong, M., & Parker, G. (2006). Reanalysis and correction of bed-load relation of meyer-peter and müller using their own database. *Journal of Hydraulic Engineering*, *132*(11), 1159–1168. https://doi.org/10.1061/(asce)0733-9429(2006)132:11(1159)

Wu, W., Shields Jr, F. D., Bennett, S. J., & Wang, S. S. (2005). A depth-averaged two-dimensional model for flow, sediment transport, and bed topography in curved channels with riparian vegetation. *Water Resources Research*, *41*(3). https://doi.org/10.1029/2004wr003730

Yager, E., Kirchner, J., & Dietrich, W. (2007). Calculating bed load transport in steep boulder bed channels. *Water Resources Research*, *43*(7). https://doi.org/10.1029/2006wr005432

Yager, E. M., Venditti, J. G., Smith, H. J., & Schmeeckle, M. W. (2018). The trouble with shear stress. *Geomorphology*, *323*, 41–50. https://doi.org/10.1016/j.geomorph.2018.09.008

You, H., & Tinoco, R. O. (2025). Characterization of porous in-stream structures to assess their implications on flow dynamics and sediment transport. *Journal of Geophysical Research: Earth Surface*, *130*(3), e2024JF007861. https://doi.org/10.1029/2024JF007861

Zhang, N., Rutherfurd, I., & Ghisalberti, M. (2019). The effect of instream logs on bank erosion potential: A flume study with multiple logs. *Journal of Ecohydraulics*, *5*(1), 57–70. https://doi.org/10.1080/24705357.2019.1669495

Zhang, N., Rutherfurd, I., & Ghisalberti, M. (2020). Effect of instream logs on bank erosion potential: A flume study with a single log. *Journal of Ecohydraulics*, *5*(1), 43–56. https://doi.org/10.1080/24705357.2019.1634499

Zhang, N., & Rutherfurd, I. D. (2020). The effect of instream logs on river-bank erosion: Field measurements of hydraulics and erosion rates. *Earth Surface Processes and Landforms*, *45*(7), 1677–1690. https://doi.org/10.1002/esp.4838